

Photometric Effects and Voronoi-diagrams as a mixed model for the spatial distribution of galaxies

L. Zaninetti

Dipartimento di Fisica , via P.Giuria 1,
I-10125 Turin,Italy

E-mail: zaninetti@ph.unito.it

Abstract. We review the model of the Voronoi Diagrams which allows to reproduce the large-scale structures of our universe as given by the astronomical catalogs. The observed number of galaxies in a given solid angle with a chosen flux/magnitude versus the redshift presents a maximum that is a function of the flux/magnitude ; it can be explained by a detailed analysis of the standard luminosity function for galaxies as well by two new luminosity function for galaxies. The current status of the research on the statistics of the Voronoi Diagrams is reviewed.

Keywords: Stochastic processes ; Distribution theory and Monte Carlo studies ; Patterns ; Structures and organization in complex systems ; Clusters of galaxies ; Cosmology

1. Introduction

During the last thirty years the spatial distribution of galaxies has been investigated from the point of view of geometrical and physical theories. One first target was to reproduce the two-point correlation function $\xi(r)$ for galaxies which on average scales as $\approx (\frac{r}{5.7Mpc})^{-1.8}$, see [1, 2]. The statistical theories of spatial galaxy distribution can be classified as

- **Levy flights:** the random walk with a variable step length can lead to a correlation function in agreement with the observed data, see [3, 4, 5, 6].
- **Percolation:** the theory of primordial explosions can lead to the formation of structures, see [7, 8]. Percolation is also used as a tool to organize : (i) the mass and galaxy distributions obtained in 3D simulations of cold dark matter (CDM) and hot dark matter (HDM), see [9], (ii) the galaxy groups and clusters in volume-limited samples of the Sloan Digital Sky Survey (SDSS), see [10]
- **Statistical approach** The statistics of the voids between galaxies was analyzed in the Center for Astrophysics Redshift survey, see [11, 12] , in the IRAS Point Source Catalog Redshift Survey (PSCz) and Updated Zwicky Catalog of Galaxies (UZC), see [13] and in the Sloan Digital Sky Survey, see [14].

The geometrical models are well represented by the concept of Voronoi Diagrams, after the two historical records by [15, 16]. The concept of Voronoi Diagrams dates back to the vortex theory applied to the solar system as developed in the 17th century, see Fig. 1 extracted from [17, 18]. The first application of the Voronoi Diagrams to the astrophysics is due to [19]. The applications of the Voronoi Diagrams to the galaxies started with [20], where a sequential clustering process was adopted in order to insert the initial seeds, and they continued with [21, 22, 23, 24, 25, 26, 27, 28, 29, 30, 31, 32, 33, 34, 35]. An updated review of the 3D Voronoi Diagrams applied to cosmology can be found in [33, 34]. The 3D Voronoi tessellation was first applied to identify groups of galaxies in the structure of a super-cluster, see [36, 37, 38, 39, 40, 41, 42]. The physical models that produce the observed properties of galaxies are intimately related, for example through the Lagrangian approximation, and can be approximately classified as

- **Cosmological N-body:** Through N-body experiments by [43] it is possible to simulate groups which are analogous to the studies of groups among bright Zwicky-catalog galaxies, see [44] or covariance functions in simulations of galaxy clustering in an expanding universe which are found to be power laws in the nonlinear regime with slopes centered on 1.9 [45]. Using gigaparticle N-body simulations to study galaxy cluster populations in Hubble volumes, [46] created mock sky surveys of dark matter structure to $z = 1.4$ over $10000^\circ sq. deg$ and to $z = 0.5$ over two full spheres. In short, N-body calculations seek to model the full nonlinear system by making discrete the matter distribution and following its evolution in a Lagrangian fashion, while N-body simulations are usually understood to concern gravity only.
- **Dynamical Models:** Starting from a power law of primordial inhomogeneities it is possible to obtain a two-point correlation function for galaxies with an exponent similar to that observed, see [47, 48, 49].

Another line of work is to assume that the velocity field is of a potential type; this assumption is called the Zel'dovich approximation, see [50, 51, 52]. The Zel'dovich

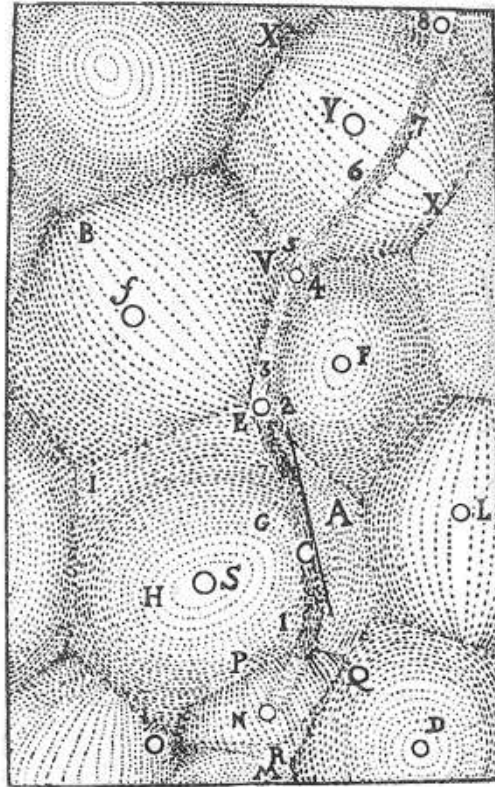


Figure 1. " God first partitioned the plenum into equal-sized portions, and then placed these bodies into various circular motions that, ultimately, formed the three elements of matter and the vortex systems" ,extracted from [17], volume III , article 46.

formalism is a Lagrangian approximation of the fully nonlinear set of equations. In this sense it is "gravity" only and does not include a pressure term.

- **The halo models:** The halo model describes nonlinear structures as virialized dark-matter halos of different mass, placing them in space according to the linear large-scale density field which is completely described by the initial power spectrum, see [53, 54, 55]. Figure 19 in [1], for example, reports the exact nonlinear model matter distribution compared with its halo-model representation.

The absence of clear information on the 3D displacement of the physical results as a function of the redshift and the selected magnitude characterize the cosmological N-body, the dynamical and the hydrodynamical models. This absence of detailed information leads to the analysis of the following questions:

- Is it possible to compare the theoretical and observational number of galaxies as a function of the redshift for a fixed flux/magnitude ?
- What is the role of the Malmquist bias when theoretical and observed numbers of galaxies versus the redshift are compared?

- Is it possible to find an algorithm which describes the intersection between a slice that starts from the center of the box and the faces of irregular Poissonian Voronoi Polyhedrons?
- Is it possible to model the intersection between a sphere of a given redshift and the faces of irregular Poissonian Voronoi Polyhedrons?
- Does the developed theory match the observed slices of galaxies as given, for example, by the 2dF Galaxy Redshift Survey?
- Does the developed algorithm explain the voids appearance in all sky surveys such as the RC3?
- Is it possible to integrate the usual probability density functions (PDFs) which characterize the main parameters of 2D and 3D Poisson Voronoi tessellation (PVT) in order to obtain an analytical expression for the survival function?
- Is it possible to model the normalized areas of $V_p(2,3)$ with the known PDFs?
- Can we transform the normalized volumes and areas into equivalent radius distributions?
- Is it possible to derive the probability density function for the radii of 2D sections in the Poissonian Voronoi Tessellation (PVT) and in a well selected case of non Poissonian Voronoi Tessellation (NPVT)?
- Is it possible to evaluate the probability of having a super-void once the averaged void's diameter is fixed?
- Is it possible to compute the correlation function for galaxies by introducing the concept of thick faces of irregular Voronoi polyhedrons?
- Is it possible to find the acoustic oscillations of the correlation function at $\approx 100Mpc$ in simulated slices of the Voronoi diagrams.

In order to answer these questions, Section 2 briefly reviews the elementary formulas adopted and Section 3 reviews the standard luminosity function for galaxies as well two new ones. The adopted catalogs as well the Malmquist bias were presented in Section 4. An accurate test of the number of galaxies as a function of the redshift is performed on the 2dF Galaxy Redshift Survey (2dFGRS), see Section 5. Section 6 reports the technique which allows us to extract the galaxies belonging to the Voronoi polyhedron. Section 7 reports the apparent distribution in effective radius of the 3D PVT as well as their associated survival functions, the fit of the normalized area distribution of the sectional PVT with the Kiang function and the exponential distribution. Section 8 reviews the probability of a plane intersecting a given sphere, the stereological approach, and then insert in the fundamental integral of the stereology the cell's radius of the new PDF. Section 9 simulates the redshift dependence of the 2dFGRS as well as the overall Third Reference Catalog of Bright Galaxies (RC3). Section 10 reports the simulation of the correlation function computed on the thick faces of the Voronoi polyhedron.

2. Useful formulas

This Section reviews the elementary cosmology adopted and the system of magnitudes.

2.1. Basic formulas

Starting from [56] the suggested correlation between expansion velocity and distance is

$$V = H_0 D = c_l z \quad , \quad (1)$$

where H_0 is the Hubble constant $H_0 = 100h \text{ km s}^{-1} \text{ Mpc}^{-1}$, with $h = 1$ when h is not specified, D is the distance in Mpc , c_l is the light velocity and z is the redshift defined as

$$z = \frac{\lambda_{obs} - \lambda_{em}}{\lambda_{em}} \quad , \quad (2)$$

with λ_{obs} and λ_{em} denoting respectively the wavelengths of the observed and emitted lines as determined from the lab source, the so called Doppler effect . Concerning the value of H_0 we will adopt a recent value as obtained by the Cepheid-calibrated luminosity of Type Ia supernovae , see [57],

$$H_0 = (62.3 \pm 5) \text{ km s}^{-1} \text{ Mpc}^{-1} \quad . \quad (3)$$

The quantity $c_l z$, a velocity , or z , a number , characterizes the catalog of galaxies.

We recall that the galaxies have peculiar velocities, making the measured redshifts a combination of cosmological redshift plus a contribution on behalf of the peculiar velocity.

The maximum redshift here considered is $z \approx 0.1$ meaning a maximum velocity of expansion of $\approx 30000 \frac{\text{Km}}{\text{s}}$; up to that value the space is assumed to be Euclidean. We now evaluate the error connected with the use of the simplest cosmological model. For a zero cosmological constant , Λ , we have the following expression for the luminosity distance D_L

$$D_L = \frac{c_l z}{H_0} \left\{ 1 + \frac{z(1 - q_0)}{\sqrt{1 + 2q_0 z + 1 + q_0 z}} \right\} \quad \text{for } \Lambda = 0 \quad , \quad (4)$$

where q_0 is the deceleration parameter, see [58, 59].

2.2. Magnitude System

The absolute magnitude of a galaxy , M , is connected to the apparent magnitude m through the relationship

$$M = m - 5 \text{Log} \left(\frac{c_l z}{H_0} \right) - 25 \quad . \quad (5)$$

In an Euclidean ,non-relativistic and homogeneous universe the flux of radiation, f , expressed in $\frac{L_\odot}{\text{Mpc}^2}$ units, where L_\odot represents the luminosity of the sun , is

$$f = \frac{L}{4\pi D^2} \quad , \quad (6)$$

where D represents the distance of the galaxy expressed in Mpc , and

$$D = \frac{c_l z}{H_0} \quad . \quad (7)$$

The relationship connecting the absolute magnitude, M , of a galaxy to its luminosity is

$$\frac{L}{L_\odot} = 10^{0.4(M_\odot - M)} \quad , \quad (8)$$

where M_{\odot} is the reference magnitude of the sun at the considered bandpass.

The flux expressed in $\frac{L_{\odot}}{Mpc^2}$ units as a function of the apparent magnitude is

$$f = 7.957 \times 10^8 e^{0.921 M_{\odot} - 0.921 m} \frac{L_{\odot}}{Mpc^2} \quad , \quad (9)$$

and the inverse relationship is

$$m = M_{\odot} - 1.0857 \ln(0.1256 \times 10^{-8} f) \quad . \quad (10)$$

The equations in this section will be used in the numerical code which allows us to simulate the large scale structures as a function of z and the selected magnitude .

3. Luminosity function for galaxies

This Section reviews the standard luminosity function for galaxies, and two new luminosity function for galaxies in the following LF .

3.1. The Schechter function

The Schechter function , introduced by [60] , provides a useful fit for the LF of galaxies

$$\Phi(L)dL = \left(\frac{\Phi^*}{L^*}\right)\left(\frac{L}{L^*}\right)^{\alpha} \exp\left(-\frac{L}{L^*}\right)dL \quad , \quad (11)$$

here α sets the slope for low values of L , L^* is the characteristic luminosity and Φ^* is the normalization. The equivalent distribution in absolute magnitude is

$$\Phi(M)dM = (0.4 \ln 10) \Phi^* 10^{0.4(\alpha+1)(M^*-M)} \exp(-10^{0.4(M^*-M)})dM \quad , \quad (12)$$

where M^* is the characteristic magnitude as derived from the data. The scaling with h is $M^* - 5 \log_{10} h$ and $\Phi^* h^3 [Mpc^{-3}]$. The joint distribution in z and f for galaxies , see formula (1.104) in [61] or formula (1.117) in [62] , is

$$\frac{dN}{d\Omega dz df} = 4\pi \left(\frac{c_l}{H_0}\right)^5 z^4 \Phi\left(\frac{z^2}{z_{crit}^2}\right) \quad , \quad (13)$$

where $d\Omega$, dz and df represent the differential of the solid angle , the redshift and the flux respectively. The critical value of z , z_{crit} , is

$$z_{crit}^2 = \frac{H_0^2 L^*}{4\pi f c_l^2} \quad . \quad (14)$$

The number of galaxies , $N_S(z, f_{min}, f_{max})$ comprised between a minimum value of flux, f_{min} , and maximum value of flux f_{max} , can be computed through the following integral

$$N_S(z) = \int_{f_{min}}^{f_{max}} 4\pi \left(\frac{c_l}{H_0}\right)^5 z^4 \Phi\left(\frac{z^2}{z_{crit}^2}\right) df \quad . \quad (15)$$

This integral does not have an analytical solution and we must perform a numerical integration.

The number of galaxies in z and f as given by formula (13) has a maximum at $z = z_{pos-max}$, where

$$z_{pos-max} = z_{crit} \sqrt{\alpha + 2} \quad , \quad (16)$$

which can be re-expressed as

$$z_{pos-max} = \frac{\sqrt{2 + \alpha} \sqrt{10^{0.4 M_{\odot} - 0.4 M^*}} H_0}{2 \sqrt{\pi} \sqrt{f} c_l} \quad . \quad (17)$$

3.2. The mass-luminosity relationship

A new LF for galaxies as derived in [63] is

$$\Psi(L)dL = \left(\frac{1}{a\Gamma(c)}\right)\left(\frac{\Psi^*}{L^*}\right)\left(\frac{L}{L^*}\right)^{\frac{c-a}{a}} \exp\left(-\left(\frac{L}{L^*}\right)^{\frac{1}{a}}\right) dL \quad , \quad (18)$$

where Ψ^* is a normalization factor which defines the overall density of galaxies , a number per cubic Mpc , $1/a$ is an exponent which connects the mass to the luminosity and c is connected with the dimensionality of the fragmentation, $c = 2d$, where d represents the dimensionality of the considered space : 1,2,3 . The scaling with h is $M^* - 5 \log_{10} h$ and $\Psi^* h^3 [Mpc^{-3}]$. The distribution in absolute magnitude is

$$\Psi(M)dM = (0.4ln10\frac{1}{a\Gamma(c)})\Psi^*10^{0.4(\frac{c}{a})(M^*-M)} \exp(-10^{0.4(M^*-M)(\frac{1}{a})})dM . \quad (19)$$

This function contains the parameters M^* , a , c and Ψ^* which are derived from the operation of fitting the observational data.

The joint distribution in z and f , in presence of the $\mathcal{M} - L$ LF (equation (18)) is

$$\frac{dN}{d\Omega dz df} = 4\pi\left(\frac{c_l}{H_0}\right)^5 z^4 \Psi\left(\frac{z^2}{z_{crit}^2}\right) . \quad (20)$$

The number of galaxies , $N_{\mathcal{M}-L}(z, f_{min}, f_{max})$ comprised between f_{min} and f_{max} , can be computed through the following integral

$$N_{\mathcal{M}-L}(z) = \int_{f_{min}}^{f_{max}} 4\pi\left(\frac{c_l}{H_0}\right)^5 z^4 \Psi\left(\frac{z^2}{z_{crit}^2}\right) df \quad , \quad (21)$$

and also in this case a numerical integration must be performed.

The number of galaxies as given by formula (20) has a maximum at $z_{pos-max}$ where

$$z_{pos-max} = z_{crit} (c + a)^{a/2} \quad , \quad (22)$$

which can be re-expressed as

$$z_{pos-max} = \frac{(a + c)^{1/2 a} \sqrt{10^{0.4 M_{\odot} - 0.4 M^*}} H_0}{2 \sqrt{\pi} \sqrt{f} c_l} . \quad (23)$$

3.3. The generalized gamma distribution with four parameters

The starting point is the probability density function (in the following PDF) named generalized gamma that we report exactly as in [64]:

$$G(x; a, b, c, k) = \frac{k \left(\frac{x-a}{b}\right)^{ck-1} e^{-\left(\frac{x-a}{b}\right)^k}}{b\Gamma(c)} \quad , \quad (24)$$

where Γ is the gamma function, a is the location parameter, b is the scale parameter, c and k are two shape parameters. A LF can be derived inserting $a = 0$, $x = L$ and $b = L^*$:

$$\Psi(L; L^*, c, k, \Psi^*) = \Psi^* \frac{k \left(\frac{L}{L^*}\right)^{ck-1} e^{-\left(\frac{L}{L^*}\right)^k}}{L^* \Gamma(c)} . \quad (25)$$

The mathematical range of existence is $0 \leq L < \infty$ and the number of parameters is four because $a = 0$ and Ψ^* have been added. The averaged luminosity is

$$\langle L \rangle = \frac{L^* \Gamma\left(\frac{1+ck}{k}\right)}{\Gamma(c)} \quad , \quad (26)$$

and the mode is at

$$L = \left(\frac{ck-1}{k}\right)^{\frac{1}{k}} L^* \quad . \quad (27)$$

The magnitude version of the LF is

$$\Psi(M)dM = \frac{\Psi^* 0.4 \ln(10) k 10^{-0.4ck(M-M^*)} e^{-10^{-0.4(M-M^*)k}}}{\Gamma(c)} dM \quad . \quad (28)$$

The mode when expressed in magnitude is at

$$M = -\frac{1.0857 \ln\left(\frac{ck-1}{k}\right)}{k} + M^* \quad . \quad (29)$$

This function contains the four parameters c , k , M^* and Ψ^* , more details as well other two new LF are reported in [65].

The joint distribution in z and f of the generalized gamma LF is

$$\frac{dN}{d\Omega dz df} = 4\pi \left(\frac{c_l}{H_0}\right)^5 z^4 \Psi\left(\frac{z^2}{z_{crit}^2}\right) \quad . \quad (30)$$

The number of galaxies, $N_{LF4}(z, f_{min}, f_{max})$ of the generalized gamma LF comprised between f_{min} and f_{max} , can be computed through the following integral:

$$N_{LF4}(z) = \int_{f_{min}}^{f_{max}} 4\pi \left(\frac{c_l}{H_0}\right)^5 z^4 \Psi\left(\frac{z^2}{z_{crit}^2}\right) df \quad , \quad (31)$$

and in this case a numerical integration must be performed.

The number of galaxies of the generalized gamma LF as given by formula (30) has a maximum at $z_{pos-max}$ where

$$z_{pos-max} = e^{1/2 \frac{\ln(1+ck) - \ln(k)}{k}} z_{crit} \quad , \quad (32)$$

which can be re-expressed as

$$z_{pos-max} = \frac{e^{1/2 \frac{\ln(1+ck) - \ln(k)}{k}} \sqrt{10^{0.4 M_{\odot} - 0.4 M^*}} H_0 k}{2 \sqrt{\pi} \sqrt{f} c_l} \quad . \quad (33)$$

4. The adopted catalogs

We now introduce the processed catalogs of galaxies, the statistics of 1024 observed cosmic voids as well the Malmquist bias.

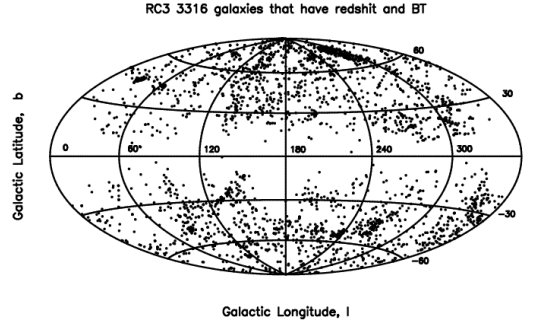


Figure 2. Hammer-Aitoff projection in galactic coordinates of 3316 galaxies in the RC3 which have BT and redshift. The ZOA is due to our own galaxy.

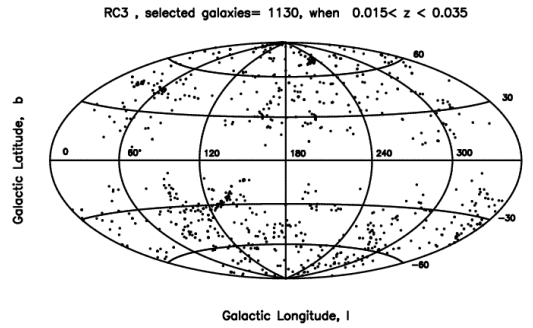


Figure 3. Hammer-Aitoff projection in galactic coordinates (observational counterpart of $V_s(2,3)$) of 1130 galaxies in the RC3 which have BT and $0.015 < z < 0.035$.

4.1. The astronomical catalogs

A first example is the 2dFGRS data release available on the web site: <http://msowww.anu.edu.au/2dFGRS/>. In particular we added together the file parent.ngp.txt which contains 145652 entries for NGP strip sources and the file parent.sgp.txt which contains 204490 entries for SGP strip sources. Once the heliocentric redshift was selected we processed 219107 galaxies with $0.001 \leq z \leq 0.3$.

A second example is the catalog RC3, see [66], which is available at the following address <http://vizier.u-strasbg.fr/viz-bin/VizieR?-source=VII/155>.

This catalog attempts to be reasonably complete for galaxies having apparent diameters larger than 1 arcmin at the D25 isophotal level and total B-band magnitudes BT, brighter than about 15.5, with a redshift not in excess of 15000 km/s. All the galaxies in the RC3 catalog which have redshift and BT are reported in Fig. 2. In the case of RC3 the covered area is 4π steradians with the exclusion of the *Zone of Avoidance (ZOA)*

Fig. 3 reports the RC3 galaxies in a given window in z . A third example is the Two-Micron All Sky Survey (2MASS) which has instruments in the infrared (1-2.2 μm) and therefore detects the galaxies in the so called "Zone of Avoidance", see [67, 68]. Fig. 4 reports a spherical cut at a given radius of the Local Super-cluster (LSC) according to 2MASS Redshift Survey (2MRS), which is available online at

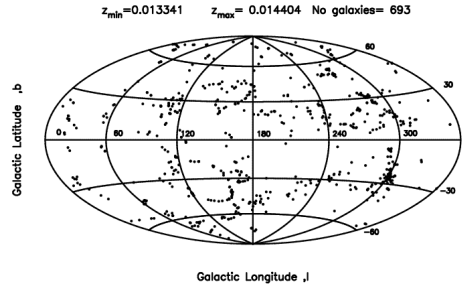


Figure 4. Hammer-Aitoff projection in galactic coordinates of a spherical cut of the Large Super Cluster data (LSC) at $0.0133 \leq z \leq 0.0144$ or $56.9 Mpc \leq D \leq 61.67$.

<https://www.cfa.harvard.edu/huchra>. In the case of 2MRS the covered area is 4π steradians.

A fourth example is the second CFA2 redshift Survey, which started in 1984, and produced slices showing that the spatial distribution of galaxies is not random but distributed on filaments that represent the 2D projection of 3D bubbles. We recall that a slice comprises all the galaxies with magnitude $m_b \leq 16.5$ in a strip of 6° wide and about 130° long. One of such slice (the so called first CFA strip) is visible at the following address <http://cfa-www.harvard.edu/~huchra/zcat/>; more details can be found in [69]. The already mentioned slice can be down-loaded from <http://cfa-www.harvard.edu/~huchra/zcat/n30.dat/>.

4.2. Statistics of the voids

The distribution of the effective radius and the radius of the maximal enclosed sphere between galaxies of the Sloan Digital Sky Survey Data Release 7 (SDSS DR7) has been reported in [14]. This catalog contains 1054 voids: Table 1 shows the basic statistical parameters of the effective radius.

4.3. Malmquist bias

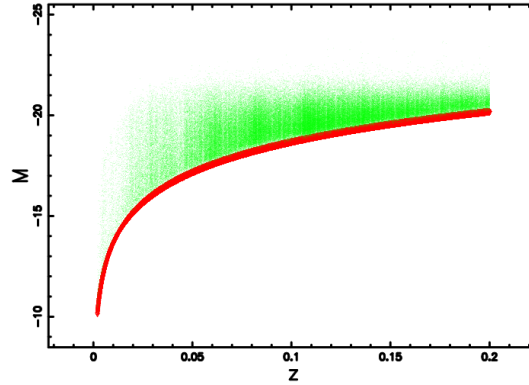
This bias was originally applied to the stars, see [70, 71], and was then applied to the galaxies by [72]. We now introduce the concept of limiting apparent magnitude and the corresponding completeness in absolute magnitude of the considered catalog as a function of redshift. The observable absolute magnitude as a function of the limiting apparent magnitude, m_L , is

$$M_L = m_L - 5 \log_{10} \left(\frac{cz}{H_0} \right) - 25 \quad . \quad (34)$$

The previous formula predicts, from a theoretical point of view, an upper limit on the absolute maximum magnitude that can be observed in a catalog of galaxies characterized by a given limiting magnitude and Fig. 5 reports such a curve and the galaxies of the 2dFGRS.

Table 1. The statistical parameters of the effective radius in SDSS DR7.

<i>parameter</i>	<i>value</i>
<i>elements</i>	1024
<i>mean</i>	$18.23h^{-1} \text{ Mpc}$
<i>variance</i>	$23.32h^{-2} \text{ Mpc}^2$
<i>standard deviation</i>	$4.82h^{-1} \text{ Mpc}$
<i>skewness</i>	0.51
<i>kurtosis</i>	0.038
<i>maximum value</i>	$34.12h^{-1} \text{ Mpc}$
<i>minimum value</i>	$9.9h^{-1} \text{ Mpc}$


Figure 5. The absolute magnitude M of 202,923 galaxies belonging to the 2dFGRS when $M_{\odot} = 5.33$ and $H_0 = 66.04 \text{ km s}^{-1} \text{ Mpc}^{-1}$ (green points). The upper theoretical curve as represented by equation (34) is reported as the red thick line when $m_L=19.61$.

The interval covered by the LF of galaxies, ΔM , is defined by

$$\Delta M = M_{max} - M_{min} \quad , \quad (35)$$

where M_{max} and M_{min} are the maximum and minimum absolute magnitude of the LF for the considered catalog. The real observable interval in absolute magnitude, ΔM_L , is

$$\Delta M_L = M_L - M_{min} \quad . \quad (36)$$

We can therefore introduce the range of observable absolute maximum magnitude expressed in percent, $\epsilon(z)$, as

$$\epsilon_s(z) = \frac{\Delta M_L}{\Delta M} \times 100\% \quad . \quad (37)$$

This is a number that represents the completeness of the sample and, given the fact that the limiting magnitude of the 2dFGRS is $m_L=19.61$, it is possible to conclude that the 2dFGRS is complete for $z \leq 0.0442$. In the case of the 2MRS the limiting

Table 2. The parameters of the Schechter function for the 2dFGRS as in Madgwick et al. 2002.

<i>parameter</i>	<i>2dFGRS</i>
$M^* - 5 \log_{10} h$ [mags]	(-19.79 ± 0.04)
α	-1.19 ± 0.01
Φ^* [$h^3 \text{ Mpc}^{-3}$]	$((1.59 \pm 0.1)10^{-2})$

Table 3. The parameters of the $\mathcal{M} - L$ LF based on the 2dFGRS data (triplets generated by the author).

	<i>2dFGRS</i>
c	0.1
$M^* - 5 \log_{10} h$ [mags]	-19 ± 0.1
Ψ^* [$h^3 \text{ Mpc}^{-3}$]	0.4 ± 0.01
a	1.3 ± 0.1

magnitude is $m_L=11.19$, and therefore the 2MRS is complete for $z \leq 0.00016$. This efficiency, expressed as a percentage, can be considered to be a version of the Malmquist bias.

5. Photometric maximum

The parameters of the Schechter LF concerning the 2dFGRS are reported in Table 2 and those of the $\mathcal{M} - L$ LF are reported in Table 3.

It is interesting to point out that other values for h different from 1 shift all absolute magnitudes by $5 \log_{10} h$ and change the number densities by the factor h^3 . Fig. 6 reports the number of observed galaxies of the 2dFGRS catalog for a given apparent magnitude and two theoretical curves as represented by formula (13) which is based on the Schechter LF and formula (20) which is based on the $\mathcal{M} - L$ LF. A similar plot can be done for the generalized gamma LF , see Fig. 7. The χ^2 analysis allows to conclude that in the two cases here examined the application of the $\mathcal{M} - L$ LF and the generalized gamma LF produce the same or better results in respect to the use of the Schechter LF. More details can be found in [73, 65].

The non-homogeneous structure of the universe can be clarified by counting the number of galaxies in one of the two slices of 2dFGRS as a function of the redshift when a sector with a central angle of 1° is considered, see Fig. 8.

Conversely, when the two slices are considered together the behavior of the number of galaxies as a function of the redshift is more continuous, see Fig. 9.

6. The 3D Voronoi Diagrams

The faces of the Voronoi Polyhedra share the same property , i.e. they are equally distant from two nuclei. The intersection between a plane and the faces produces

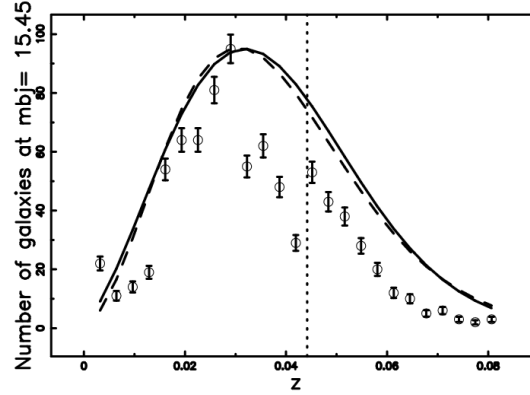


Figure 6. The galaxies of the 2dFGRS with $15.27 \leq bJmag \leq 15.65$ or $59253 \frac{L_{\odot}}{Mpc^2} \leq f \leq 83868 \frac{L_{\odot}}{Mpc^2}$ (with $bJmag$ representing the relative magnitude used in object selection), are isolated in order to represent a chosen value of m and then organized in frequencies versus heliocentric redshift, (empty circles); the error bar is given by the square root of the frequency. The maximum in the frequencies of observed galaxies is at $z = 0.03$. The theoretical curve generated by the Schechter LF (formula (13) and parameters as in column 2dFGRS of Table 2) is drawn (full line). The theoretical curve generated by the $\mathcal{M} - L$ LF (formula (20) and parameters as in column 2dFGRS of Table 3) is drawn (dashed line); $\chi^2 = 550$ for the Schechter function and $\chi^2 = 503$ for the $\mathcal{M} - L$ function. In this plot $\mathcal{M}_{\odot} = 5.33$ and $h=0.623$. The vertical dotted line represents the boundary between complete and incomplete samples.

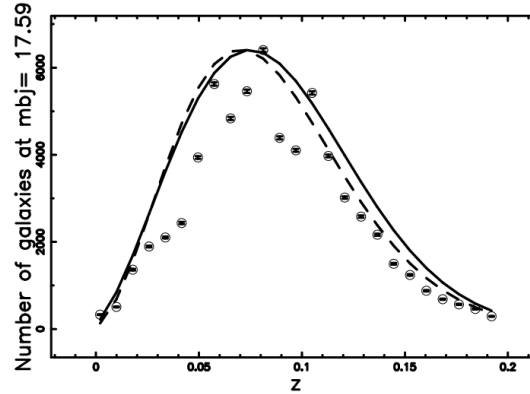


Figure 7. The galaxies of the 2dFGRS database with $16.77 \leq bJmag \leq 18.40$ or $4677 \frac{L_{\odot}}{Mpc^2} \leq f \leq 21087 \frac{L_{\odot}}{Mpc^2}$ (with $bJmag$ representing the relative magnitude used in object selection), are isolated in order to represent a chosen value of m and then organized as frequency versus heliocentric redshift, (empty circles); the error bar is given by the square root of the frequency. The maximum in the frequencies of observed galaxies is at $z = 0.085$ when $\mathcal{M}_{\odot} = 5.33$ and $h=1$. The theoretical curve generated by the Schechter function of luminosity (formula (13) and parameters as in column 2dFGRS of Table 2) is drawn (full line). The theoretical curve generated by generalized gamma LF , formula (30), and parameters as in column 2dFGRS of Table 3) is drawn (dashed line); $\chi^2 = 8078$ for the Schechter function and $\chi^2 = 6654$ for generalized gamma LF .

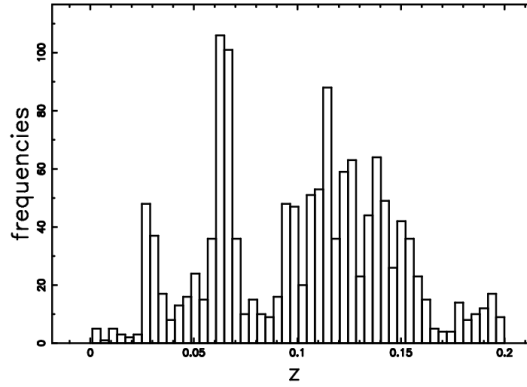


Figure 8. Histogram (step-diagram) of the number of galaxies of 2dFGRS as a function of the redshift in the slice to the right of Fig. 23, the number of bins is 50. The circular sector has a central angle of 1° .

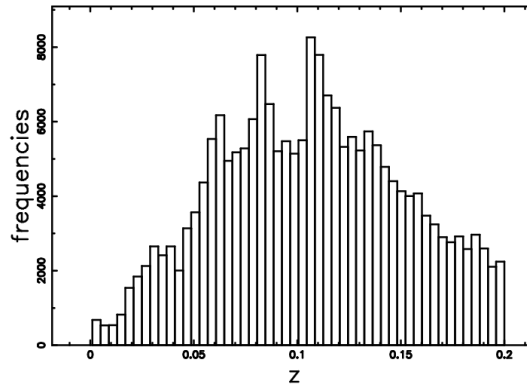


Figure 9. Histogram (step-diagram) of the number of galaxies of 2dFGRS as a function of the redshift when the two slices of Fig. 23 are added together, the number of bins is 50.

diagrams which are similar to the edges' displacement in 2D Voronoi diagrams. From the point of view of the observations it is very useful to study the intersection between a slice which crosses the center of the box and the faces of irregular polyhedrons where presumably the galaxies reside. The general definition of the 3D Voronoi Diagrams is given in Section 6.1. The intersection between a slice of a given opening angle, for example 3° , and the faces of the Voronoi Polyhedra can be realized through an approximate algorithm, see next Section 6.2.

6.1. General Definition

The Voronoi diagram for a set of seeds, S , located at position x_i in \mathcal{R}^3 space is the partitioning of that space into regions such that all locations within any one region are closer to the generating point than to any other. In the following we will work on a three dimensional lattice defined by $pixels \times pixels \times pixels$ points, L_{kmn} . The Voronoi polyhedron V_i around a given center i , is the set of lattice points L_{kmn} closer

to i than to any j : more formally,

$$L_{kmn} \in V_i \leftrightarrow |x_{kmn} - x_i| \leq |x_{kmn} - x_j| \quad , \quad (38)$$

where x_{kmn} denotes the lattice point position. Thus, the Polyhedra are intersections of half-spaces. Given a center i and its neighbor j , the line ij is cut perpendicularly at its midpoint y_{ij} by the plane h_{ij} . H_{ij} is the half-space generated by the plane h_{ij} , which consists of the subset of lattice points on the same side of h_{ij} as i ; therefore

$$V_i = \cap_j H_{ij}, \quad (39)$$

V_i is bounded by faces, with each face f_{ij} belonging to a distinct plane h_{ij} . Each face will be characterized by its vertexes and edges.

6.2. The adopted algorithm

Our method considers a 3D lattice with $pixels^3$ points: present in this lattice are N_s seeds generated according to a random process. All the computations are usually performed on this mathematical lattice; the conversion to the physical lattice is obtained by multiplying the unit by $\delta = \frac{side}{pixels-1}$, where $side$ is the length of the cube expressed in the physical unit adopted. In order to minimize boundary effects introduced by those polyhedron which cross the cubic boundary, the cube in which the seeds are inserted is amplified by a factor *amplify*. Therefore the N_s seeds are inserted in a volume $pixels^3 \times amplify$, which is bigger than the box over which the scanning is performed; *amplify* is generally taken to be equal to 1.2. This procedure inserts periodic boundary conditions to our cube. A sensible and solid discussion of what such an extension of a cube should be can be found in [74]. The set S of the seeds can be of Poissonian or non-Poissonian type. Adopting the point of view that the universe should be the same from each point of view of the observer the Poissonian seeds can represent the best choice in order to reproduce the large scale structures.

The Poissonian seeds are generated independently on the X , Y and Z axis in 3D through a subroutine which returns a pseudo-random real number taken from a uniform distribution between 0 and 1. For practical purposes, the subroutine RAN2 was used, see [75]. Particular attention should be paid to the average observed diameter of voids, \overline{DV}^{obs} , here chosen as

$$\overline{DV}^{obs} \approx 36.46 Mpc/h \quad , \quad (40)$$

see Section 4.2. The number of Poissonian seeds is chosen in such a way that the averaged volume occupied by a Voronoi polyhedron is equal to the averaged observed volume of the voids in the spatial distribution of galaxies; more details can be found in [35].

We now work on a 3D lattice $L_{k,m,n}$ of $pixels^3$ elements. Given a section of the cube (characterized, for example, by $k = \frac{pixels}{2}$) the various V_i (the volume belonging to the seed i) may or may not cross the pixels belonging to the two dimensional lattice. A typical example of a 2D cut organized in two strips about 75° long is visible in Fig. 10 where the Cartesian coordinates X and Y with the origin of the axis at the center of the box has been used. The previous cut has an extension on the Z -axis equal to zero. Conversely Fig. 11 reports two slices of 75° long and 3° wide. In this case the extension of the enclosed region belonging to the Z -axis increases with distance according to

$$\Delta Z = \sqrt{X^2 + y^2} \tan \frac{\alpha}{2} \quad , \quad (41)$$

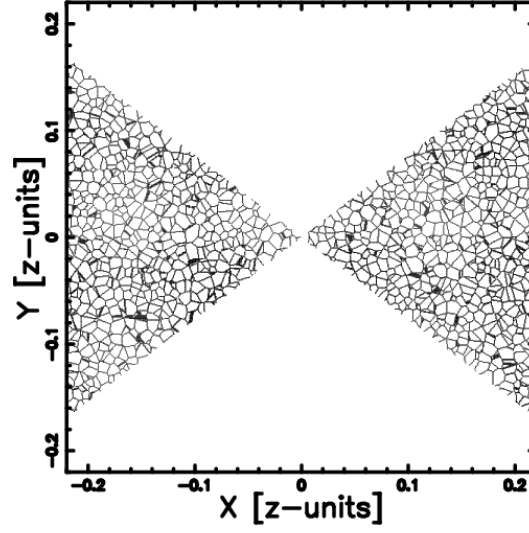


Figure 10. Portion of the Poissonian Voronoi-diagram $V_p(2,3)$; cut on the X-Y plane when two strips of 75° are considered. The parameters are $pixels=600$, $N_s = 137998$, $side = 131908 \text{ Km/sec}$ and $amplify = 1.2$.

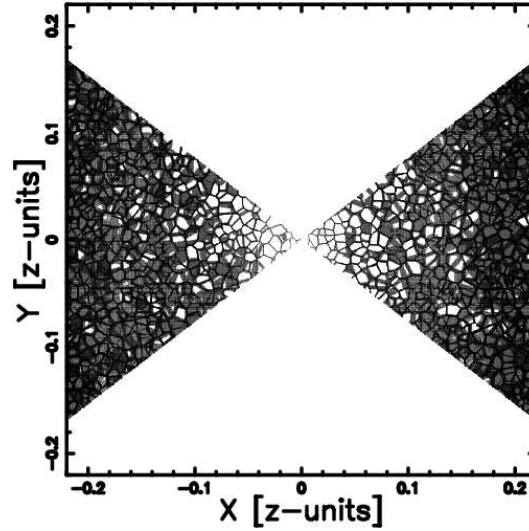


Figure 11. The same as Fig. 10 but now two slices of 75° long and 3° wide are considered.

where ΔZ is the thickness of the slice and α is the opening angle, in our case 3° . In order to simulate the slices of observed galaxies a subset is extracted (randomly chosen) of the pixels belonging to a slice as represented, for example, in Fig. 11. In this operation of extraction of the galaxies from the pixels of the slice, the photometric rules as represented by formula (13) must be respected.

The cross sectional area of the VP can also be visualized through a spherical cut

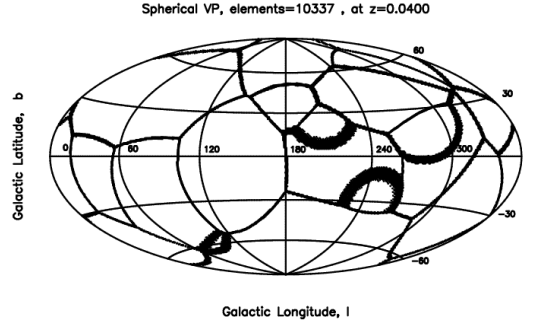


Figure 12. The Voronoi-diagram $V_s(2,3)$ in the Hammer-Aitoff projection at $z = 0.04$. The parameters are $pixels = 400$, $N_s = 137998$, $side = 131908 \text{ Km/sec}$ and $amplify = 1.2$.

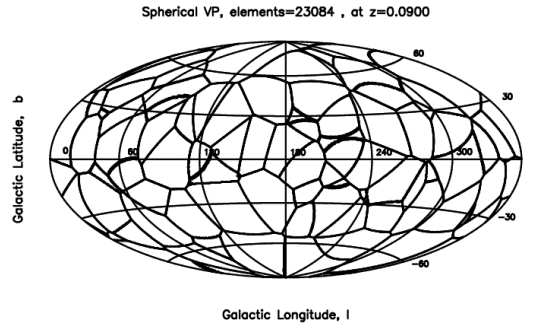


Figure 13. The Voronoi-diagram $V_s(2,3)$ in the Hammer-Aitoff projection at $z = 0.09$; other parameters as in Fig. 12.

characterized by a constant value of the distance to the center of the box, in this case expressed in z units, see Fig. 12 and Fig. 13; this intersection is called $V_s(2,3)$ where the index s stands for sphere.

7. The statistics of the Voronoi Diagrams

A probability density function (PDF) is the first derivative of a distribution function (DF) $F(x)$ with respect to x . In the case where the PDF is known but the DF is unknown, the following integral is evaluated

$$F(x) = \int_0^x f(x)dx \quad . \quad (42)$$

As a consequence the survival function (SF) is

$$SF = 1 - F(x) \quad . \quad (43)$$

We recall that the PVT is a particular case of the Voronoi tessellation in which the seeds are generated independently on the X , Y and Z axes in 3D.

7.1. The Kiang function

The gamma variate $H(x; c)$ ([19]) is

$$H(x; c) = \frac{c}{\Gamma(c)} (cx)^{c-1} \exp(-cx) \quad , \quad (44)$$

where $0 \leq x < \infty$, $c > 0$, and $\Gamma(c)$ is the gamma function with argument c . The Kiang PDF has a mean of

$$\mu = 1 \quad , \quad (45)$$

and variance

$$\sigma^2 = \frac{1}{c} \quad . \quad (46)$$

This PDF can be generalized by introducing the dimension of the considered space, $d(d = 1, 2, 3)$, and $c = 2d$

$$H(x; d) = \frac{2d}{\Gamma(2d)} (2dx)^{2d-1} \exp(-2dx) \quad . \quad (47)$$

In the case of a 1D PVT, $c = 2$ is an exact analytical result and conversely c is supposed to be 4 or 6 for 2D or 3D PVTs, respectively, [19]. The DF of the Kiang function, DF_K , is

$$DF_K = 1 - \frac{\Gamma(c, cx)}{\Gamma(c)} \quad , \quad (48)$$

where the incomplete Gamma function, $\Gamma(a, z)$, is defined by

$$\Gamma(a, z) = \int_z^\infty e^{-t} t^{a-1} dt \quad . \quad (49)$$

The survival function S_K is

$$S_K = \frac{\Gamma(c, cx)}{\Gamma(c)} \quad . \quad (50)$$

7.2. Generalized gamma

The generalized gamma PDF with three parameters a, b, c , [76, 77, 78], is

$$f(x; b, c, d) = c \frac{b^{a/c}}{\Gamma(a/c)} x^{a-1} \exp(-bx^c) \quad . \quad (51)$$

The generalized gamma has a mean of

$$\mu = \frac{b^{-\frac{1}{c}} \Gamma(\frac{1+a}{c})}{\Gamma(\frac{a}{c})} \quad , \quad (52)$$

and a variance of

$$\sigma^2 = \frac{b^{-\frac{2}{c}} \left(+\Gamma(\frac{2+a}{c}) \Gamma(\frac{a}{c}) - (\Gamma(\frac{1+a}{c}))^2 \right)}{(\Gamma(\frac{a}{c}))^2} \quad . \quad (53)$$

The SF of the generalized gamma is

$$S_{GG} = \frac{\Gamma(\frac{a}{c}, bx^c)}{\Gamma(\frac{a}{c})} \quad . \quad (54)$$

7.3. Ferenc–Neda function

A new PDF has been recently introduced, [77], in order to model the normalized area/volume in a 2D/3D PVT

$$FN(x; d) = C \times x^{\frac{3d-1}{2}} \exp(-(3d+1)x/2) \quad , \quad (55)$$

where C is a constant,

$$C = \frac{\sqrt{2}\sqrt{3d+1}}{2 \cdot 2^{3/2d} (3d+1)^{-3/2d} \Gamma(3/2d+1/2)} \quad , \quad (56)$$

and $d(d=1, 2, 3)$ is the dimension of the space under consideration. We will call this function the Ferenc–Neda PDF; it has a mean of

$$\mu = 1 \quad , \quad (57)$$

and variance

$$\sigma^2 = \frac{2}{3d+1} \quad . \quad (58)$$

The SF of the Ferenc–Neda function when $d=3$ is

$$S_{FN3} = e^{-5x} + 5e^{-5x}x + \frac{25}{2}e^{-5x}x^2 + \frac{125}{6}e^{-5x}x^3 + \frac{625}{24}x^4e^{-5x} \quad . \quad (59)$$

7.4. Kiang function of the radius

We now analyze the distribution in effective radius R of the 3D PVT. We assume that the volume of each cell, v , is

$$v = \frac{4}{3}\pi\left(\frac{R}{\rho}\right)^3 \quad , \quad (60)$$

where ρ is a length that connects the normalized radius to the observed one. In the following, we derive the PDF for radius and related quantities relative to the Kiang function and Ferenc–Neda function. The PDF, $H_R(R; c)$, of the radius corresponding to the Kiang function as represented by (44) is

$$H_R(R; c) = \frac{4c \left(4/3 \frac{c\pi R^3}{\rho^3}\right)^{c-1} e^{-4/3 \frac{c\pi R^3}{\rho^3}} \pi R^2}{\Gamma(c) \rho^3} \quad , \quad (61)$$

where $0 \leq R < \infty$, $c > 0$ and $\rho > 0$. The Kiang PDF of the radius has a mean of

$$\mu = 1/2 \frac{\sqrt[3]{2}\sqrt[3]{3}\Gamma(1/3+c)}{\sqrt[3]{c}\sqrt[3]{\pi}\Gamma(c)} \rho \quad , \quad (62)$$

and variance

$$\sigma^2 = \frac{1}{4} \frac{3^{\frac{2}{3}} 2^{\frac{2}{3}} (\Gamma(2/3+c)\Gamma(c) - (\Gamma(1/3+c))^2)}{c^{2/3} \pi^{2/3} (\Gamma(c))^2} \rho^2 \quad . \quad (63)$$

The survival function of the Kiang function in radius is

$$S_{KR} = \frac{\Gamma\left(c, 4/3 c\pi \left(\frac{R}{\rho}\right)^3\right)}{\Gamma(c)} \quad . \quad (64)$$

Table 4. Values of χ^2 for the cell normalized area-distribution function of $V_p(2, 3)$; here T_i are the theoretical frequencies and O_i are the sample frequencies. Here we have 8517 Poissonian seeds and 40 intervals in the histogram.

<i>PDF</i>	<i>parameters</i>	χ^2
$H(x; c)$ (Eq.(44))	$c = 2.07$	114.41
$p(x; b)$ (Eq.(73))	$d = 1$	85.38

7.5. The Ferenc–Neda function of the radius

The PDF as a function of the radius, obtained from (55) and inserting $d = 3$, is

$$FN_R(R; d) = \frac{400000 \pi^5 R^{14} e^{-\frac{20}{3} \frac{\pi R^3}{\rho^3}}}{243 \rho^{15}} . \quad (65)$$

The mean of the Ferenc–Neda function is

$$\mu = 0.6\rho , \quad (66)$$

and the variance is

$$\sigma^2 = 0.0085\rho^2 . \quad (67)$$

The SF of the Ferenc–Neda function of the radius when $d = 3$ is

$$\begin{aligned} S_{FN3R} = & e^{-\frac{20}{3} \frac{\pi R^3}{\rho^3}} + \frac{20}{3} e^{-\frac{20}{3} \frac{\pi R^3}{\rho^3}} R^3 \pi \rho^{-3} + \frac{200}{9} e^{-\frac{20}{3} \frac{\pi R^3}{\rho^3}} R^6 \pi^2 \rho^{-6} \\ & + \frac{4000}{81} e^{-\frac{20}{3} \frac{\pi R^3}{\rho^3}} R^9 \pi^3 \rho^{-9} + \frac{20000}{243} e^{-\frac{20}{3} \frac{\pi R^3}{\rho^3}} R^{12} \pi^4 \rho^{-12} . \end{aligned} \quad (68)$$

7.6. Kiang distribution of $V_p(2, 3)$ in radius

Here, we first model the normalized area-distribution $V_p(2, 3)$ with Kiang PDFs as represented by (44), see Table 4.

The PDF, $H_{R23}(R; c)$, as a function of the radius corresponding to the Kiang function as represented by (44) for $V_p(2, 3)$ is

$$H_{R23}(R; c) = \frac{2c \left(\frac{c\pi R^2}{\rho^2} \right)^{c-1} e^{-\frac{c\pi R^2}{\rho^2}} \pi R}{\Gamma(c) \rho^2} , \quad (69)$$

where $0 \leq R < \infty$, $c > 0$ and $\rho > 0$. The Kiang PDF of the radius for $V_p(2, 3)$ has a mean of

$$\mu = \frac{\rho \Gamma(c + 1/2)}{\sqrt{c} \sqrt{\pi} \Gamma(c)} , \quad (70)$$

and variance

$$\sigma^2 = \frac{\rho^2 \left(c(\Gamma(c))^2 - (\Gamma(c + 1/2))^2 \right)}{c\pi (\Gamma(c))^2} . \quad (71)$$

The survival function of the Kiang function, S_{KR23} , in radius for $V_p(2, 3)$ is

$$S_{KR23} = \frac{\Gamma\left(c, 2 \frac{c\pi R^2}{\rho^2}\right)}{\Gamma(c)} . \quad (72)$$

A comparison of the survival function S_{KR23} of the radius and the exponential distribution is reported in Fig. 14.

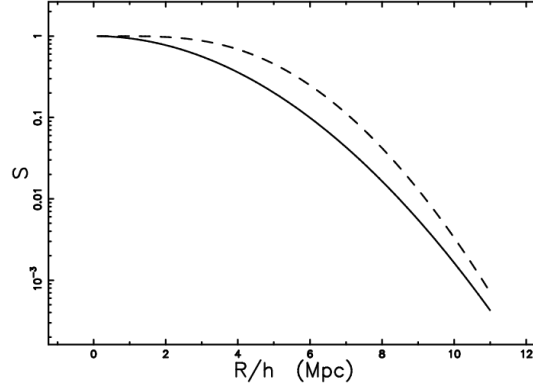


Figure 14. The survival function, S_{KR23} , of the radius of the Kiang function for $V_p(2,3)$ as represented by (72) when $\rho = 13$ Mpc, $c = 2.25$ and $\chi^2 = 67.1$ with 100 points (dashed line). The survival function, S_{ER23} , of the radius of the exponential distribution for $V_p(2,3)$ as represented by (78) when $\rho = 7$ Mpc and $\chi^2 = 9.27$ with 100 points (full line).

7.7. Exponential distribution of $V_p(2,3)$ in radius

Another PDF that can be considered in order to model the normalized area distribution of $V_p(2,3)$ is the exponential distribution,

$$p(x) = \frac{1}{b} \exp -\frac{x}{b} \quad , \quad (73)$$

which has an average value

$$\bar{x} = b \quad . \quad (74)$$

In the case of the normalized areas $b = 1$, Table 4 reports the χ^2 values of the two distributions adopted here. The PDF, $p_{R23}(R; c)$, as a function of the radius corresponding to the exponential distribution as represented by (73) for $V_p(2,3)$ is

$$p_{R23}(R; c) = \frac{2 e^{-\frac{\pi R^2}{\rho^2}} \pi R}{\rho^2} \quad , \quad (75)$$

where $0 \leq R < \infty$, $\rho > 0$. The exponential PDF of the radius for $V_p(2,3)$ has a mean of

$$\mu = \frac{\pi^{3/2}}{2 \rho^2 \left(\frac{\pi}{\rho^2}\right)^{3/2}} \quad , \quad (76)$$

and variance

$$\sigma^2 = \frac{\rho^2 (4 - \pi)}{4 \pi} \quad . \quad (77)$$

The survival function of the exponential distribution, S_{ER23} , in radius for $V_p(2,3)$ is

$$S_{ER23} = e^{-\frac{\pi R^2}{\rho^2}} \quad . \quad (78)$$

Fig. 14 reports a comparison between the survival function of Kiang distribution and the exponential distribution for $V_p(2,3)$. More details can be found in [79].

8. Stereology

We first briefly review how a PDF $f(x)$ changes to $g(y)$ when a new variable $y(x)$ is introduced. We limit ourselves to the case in which $y(x)$ is a one-to-one transformation. The rule for transforming a PDF is

$$g(y) = \frac{f(x)}{\left|\frac{dy}{dx}\right|}. \quad (79)$$

Analytical results have shown that sections through D-dimensional Voronoi tessellations are not themselves D-1 Voronoi tessellations, see [80, 81, 82]. According to [83], the probability of a plane intersecting a given sphere is proportional to the sphere's radius, R . Cross-sections of radius r may be obtained from any sphere with a radius greater than or equal to r . We may now write a general expression for the probability of obtaining a cross-section of radius r from the whole distribution (which is denoted $F(R)$):

$$f(r) = \int_r^\infty F(R) R \frac{1}{R} \frac{r}{\sqrt{R^2 - r^2}} dR, \quad (80)$$

which is formula (A7) in [83]. That is to say, $f(r)$ is the probability of finding a bubble of radius R , multiplied by the probability of intersecting this bubble, multiplied by the probability of obtaining a slice of radius r from this bubble, integrated over the range of $R \geq r$. A first example is given by the so called monodisperse bubble size distribution (BSD) which are bubbles of constant radius R and therefore

$$F(R) = \frac{1}{R}, \quad (81)$$

which is defined in the interval $[0, R]$ and

$$f(r) = \frac{r}{\sqrt{R^2 - r^2} R}, \quad (82)$$

which is defined in the interval $[0, R]$, see Eq. (A4) in [83]. The average value of the radius of the 2D-slices is

$$\bar{r} = 1/4 R\pi, \quad (83)$$

the variance is

$$\sigma^2 = 2/3 R^2 - 1/16 R^2 \pi^2, \quad (84)$$

and finally,

$$\text{Skewness} = -1.151, \quad \text{Kurtosis} = 0.493. \quad (85)$$

8.1. PVT stereology

In order to find our $F(R)$, we now analyze the distribution in effective radius R of the 3D PVT. We assume that the volume of each cell, v , is

$$v = \frac{4}{3}\pi R^3. \quad (86)$$

In the following, we derive the PDF for the radius and related quantities relative to the Ferenc-Neda function. The PDF as a function of the radius according to the rule of change of variables (79), is obtained from (55) on inserting $d = 3$ and was already defined, see equation 65. The average radius is

$$\bar{R} = 0.6065, \quad (87)$$

Table 5. The parameters of $f(r)$, Eq. (91), relative to the *PVT* case.

<i>Parameter</i>	<i>value</i>
<i>Mean</i>	0.4874
<i>Variance</i>	0.02475
<i>Mode</i>	0.553
<i>Skewness</i>	-.5229
<i>Kurtosis</i>	-.1115

and the variance is

$$\sigma^2(R) = 0.00853. \quad (88)$$

The introduction of the scale factor, b , with the new variable $R = R'/b$ transforms Eq. (65) into

$$F(R', b) = \frac{400000 \pi^5 R'^{14} e^{-\frac{20}{3} \frac{\pi R'^3}{b^3}}}{243 b^{15}}. \quad (89)$$

We now have $F(R)$ as given by Eq. (65) and the fundamental integral (80), as derived in [84], is

$$f(r) = 2/3 K \sqrt[6]{3} \sqrt[3]{10} \sqrt[3]{\pi} r G_{3,5}^{4,1} \left(\frac{100}{9} \pi^2 r^6 \left| \begin{matrix} 5/6, 1/6, 1/2 \\ 7/3, 2/3, 1/3, 0, \frac{17}{6} \end{matrix} \right. \right) \quad (90)$$

$$0 \leq r \leq 1,$$

where K is a constant,

$$K = 1.6485, \quad (91)$$

and the Meijer G -function is defined as in [85, 86, 87]. Details on the real or complex parameters of the Meijer G -function are given in the Appendix of [88]. Table 5 shows the average value, variance, mode, skewness, and kurtosis of the already derived $f(r)$. Asymptotic series are

$$f(r) \sim 2.7855 r \quad (92)$$

when $r \rightarrow 0$,

and

$$f(r) \sim -0.006 (r - 1) + 0.136 (r - 1)^2 \quad (93)$$

when $r \rightarrow 1$.

The distribution function (DF) is

$$DF(r) = \frac{1}{90} K 3^{5/6} 10^{2/3} G_{4,6}^{4,2} \left(\frac{100}{9} \pi^2 r^6 \left| \begin{matrix} 1, 7/6, 1/2, 5/6 \\ 8/3, 1, 2/3, 1/3, \frac{19}{6}, 0 \end{matrix} \right. \right) \frac{1}{\sqrt[3]{\pi}} \quad (94)$$

$$0 \leq r \leq 1.$$

The already defined PDF is defined in the interval $0 \leq r \leq 1$. In order to make a comparison with a normalized sample which has a unitarian mean or an astronomical

Table 6. Parameters of $f(x,b)$, Eq. (96), relative to the *PVT* case.

<i>Parameter</i>	$b = 2.051$	$b = 34$
<i>Mean</i>	1.	16.57Mpc
<i>Variance</i>	0.104	28.62Mpc ²
<i>Mode</i>	1.134	18.80Mpc

Table 7. The values of χ^2 for the cell normalized area-distribution of $V_p(2,3)$. The number of 2D cells is 789, the 3D seeds are 15 000 and the number of bins in the histogram is 30.

<i>PDF</i>	<i>parameters</i>	χ^2
$H(x; c)$ (Eq. (44))	$c = 5.8$	250.8
$f(x; d)$ (Eq. (55))	$d = 3.53$	250.8
$f(x, b)$ (Eq. (96))	$b = 2.0514$	127

sample which has the mean expressed in Mpc, a transformation of scale should be introduced. The change of variable is $r = x/b$ and the resulting PDF is

$$f(x, b) = \frac{2}{3} K \sqrt[6]{3} \sqrt[3]{10} \sqrt[3]{\pi x} G_{3,5}^{4,1} \left(\frac{100}{9} \frac{\pi^2 x^6}{b^6} \middle| \begin{matrix} 5/6, 1/6, 1/2 \\ 7/3, 2/3, 1/3, 0, \frac{17}{6} \end{matrix} \right) \left(\frac{1}{b} \right)^2 \quad (95)$$

$$0 \leq r \leq b.$$

As an example, Table 6 shows the statistical parameters for two different values of b . Skewness and kurtosis do not change with a transformation of scale.

We briefly recall that a PDF $f(x)$ is the first derivative of a distribution function (DF) $F(x)$ with respect to x . When the DF is unknown but the PDF known, we have

$$F(x) = \int_0^x f(x) dx. \quad (96)$$

The survival function (SF) $S(x)$ is

$$S(x) = 1 - F(x), \quad (97)$$

and represents the probability that the variate takes a value greater than x . The SF with the scaling parameter b is

$$SF(x, b) = 1 - 0.01831 3^{5/6} 10^{2/3} G_{4,6}^{4,2} \left(\frac{100}{9} \frac{x^6 \pi^2}{b^6} \middle| \begin{matrix} 1, 7/6, 1/2, 5/6 \\ 8/3, 1, 2/3, 1/3, \frac{19}{6}, 0 \end{matrix} \right) \frac{1}{\sqrt[3]{\pi}} \quad (98)$$

$$0 \leq r \leq b.$$

A first application can be a comparison between the real distribution of radii of $V_p(2,3)$, see Fig. 15, and the already obtained rescaled PDF $f(x, b)$. The fit with the rescaled $f(x, b)$ is shown in Fig. 16 and Table 7 shows the χ^2 of three different fitting functions.

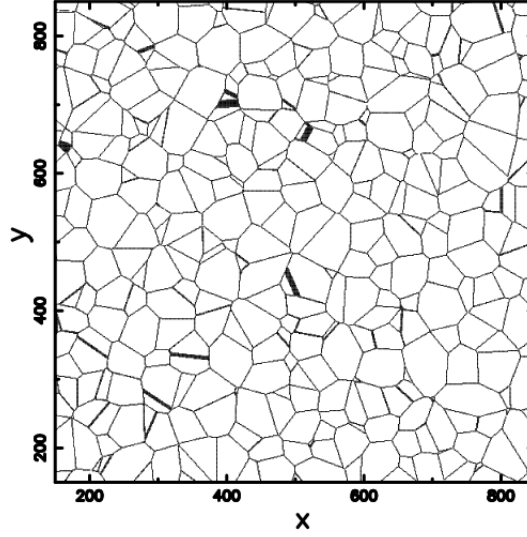


Figure 15. PVT diagram $V_p(2,3)$ when 789 2D cells generated by 15 000 3D seeds are considered.

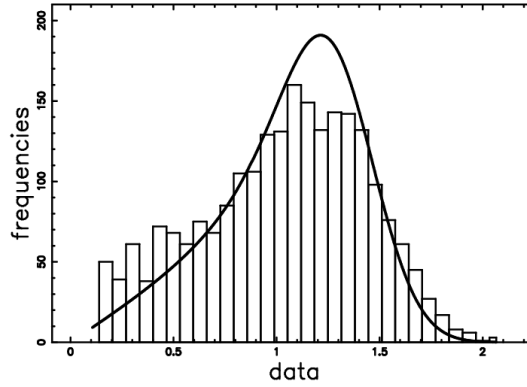


Figure 16. Histogram (step-diagram) of PVT $V_p(2,3)$ when 789 2D cells, generated by 15 000 3D seeds, are considered. The superposition of the $f(x, b)$, Eq. (96), is displayed.

The PDF f_A of the areas of $V_p(2,3)$ can be obtained from $f(r)$ by means of the transformation, see [84],

$$f_A(A) = f(r) \left(\left(\frac{A}{\pi} \right)^{1/2} \right) \frac{\pi^{-1/2}}{2} A^{-1/2}, \quad (99)$$

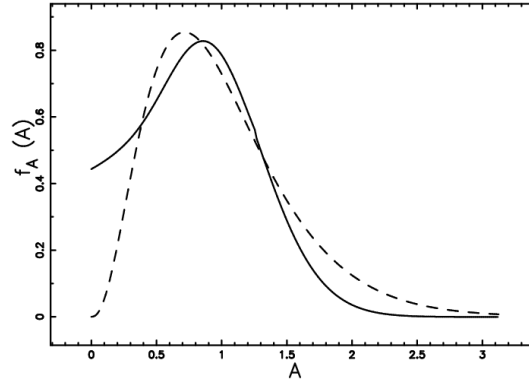
that is,

$$f_A(A) = 0.549 \sqrt[6]{3} \sqrt[3]{10} G_{3,5}^{4,1} \left(\frac{100}{9} \frac{A^3}{\pi} \left| \begin{matrix} 5/6, 1/6, 1/2 \\ 7/3, 2/3, 1/3, 0, \frac{17}{6} \end{matrix} \right. \right) \pi^{-2/3}. \quad (100)$$

The already derived $f_A(A)$ has average value, variance, mode, skewness and kurtosis as shown in Table 8.

Table 8. Parameters of $f_A(A)$, Eq. (100), relative to the *PVT* case.

Parameter	value
Mean	0.824
Variance	0.204
Mode	0.858
Skewness	0.278
Kurtosis	-0.337


Figure 17. The PDF f_A , Eq. (100), as a function of A (full line) and $FN(x;d)$, Eq. (55), when $d=2$ (dotted line).

Since, for r close to 0, $f(r) \sim r$ from Eq. (100) it follows that $f_A(0) \neq 0$, in particular $f_A(0) = 0.443$ and Fig. 17 shows the graph of f_A .

The previous figure shows that sections through 3-dimensional Voronoi tessellations are not themselves 2-dimensional Voronoi tessellations because $f_A(0)$ has a finite value rather than 0 as does the 2D area distribution; this fact can be considered a numerical demonstration in agreement with [82]. The distribution function F_A is given by

$$F_A = 0.018 \, 3^{5/6} 10^{2/3} G_{4,6}^{4,2} \left(\frac{100}{9} \frac{A^3}{\pi} \left| \begin{matrix} 1, 7/6, 1/2, 5/6 \\ 8/3, 1, 2/3, 1/3, \frac{19}{6}, 0 \end{matrix} \right. \right) \frac{1}{\sqrt[3]{\pi}}. \quad (101)$$

Consider a three-dimensional Poisson Voronoi diagram and suppose it intersects a randomly oriented plane γ : the resulting cross sections are polygons.

A comparison between F_A and the area of the irregular polygons is shown in Fig. 18. In this case the number of seeds is 300000 and we processed 100168 irregular polygons obtained by adding together results of cuts by 41 triples of mutually perpendicular planes. The maximum distance between the two curves is $d_{max} = 0.039$.

As concerns the linear dimension, in our approximation the two-dimensional cells were considered circles and thus, for consistency, the radius r of an irregular polygon was defined as

$$r = \left(\frac{A}{\pi} \right)^{1/2}, \quad (102)$$

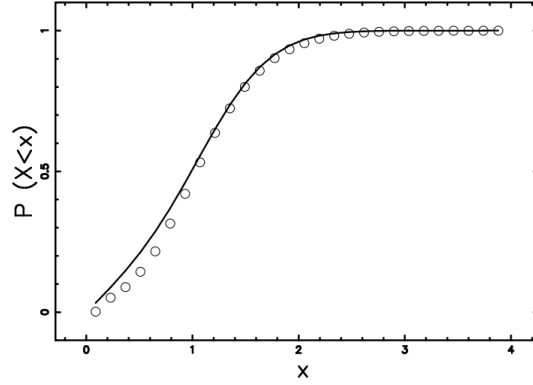


Figure 18. Comparison between data (empty circles) and theoretical curve (continuous line) of the distribution of areas of the planar cross sections.

that is, r is the radius of a circle with the same area, A , as the polygon. The assumption of sphericity can be considered an axiom of the theory here presented, but for a more realistic situation the stereological results will be far more complex. More details can be found in [88]

8.2. NPVT stereology

An example of NPVT is represented by a distribution in volume which follows a Kiang function as given by Eq. (44). The case of PVT volumes indicates $c = 5$, or $c = 6$, the so called Kiang conjecture: we will take c as a variable. The resulting distribution in radius once the scaling parameter b is introduced is

$$F_K(R, b, c) = \frac{4c \left(4/3 \frac{c\pi R^3}{b^3}\right)^{c-1} e^{-4/3 \frac{c\pi R^3}{b^3}} \pi R^2}{\Gamma(c) b^3}. \quad (103)$$

The average radius is

$$\bar{R} = \frac{\sqrt[3]{2} \sqrt[3]{3} b \Gamma(1/3 + c)}{2 \sqrt[3]{c} \sqrt[3]{\pi} \Gamma(c)}, \quad (104)$$

and the variance is

$$\sigma^2(R) = \frac{-3^{2/3} 2^{2/3} b^2 \left(-\Gamma(2/3 + c) \Gamma(c) + (\Gamma(1/3 + c))^2\right)}{4c^{2/3} \pi^{2/3} (\Gamma(c))^2}. \quad (105)$$

The skewness is

$$\gamma = \frac{(\Gamma(c))^3 c - 3\Gamma(c) \Gamma(1/3 + c) \Gamma(2/3 + c) + 2(\Gamma(1/3 + c))^3}{\left(\Gamma(2/3 + c) \Gamma(c) - (\Gamma(1/3 + c))^2\right)^{3/2}}, \quad (106)$$

and the kurtosis is given by a complicated analytical expression. Fig. 19 shows a superposition of the effective radii of the voids in SDSS DR7 with a superposition of the curve of the theoretical PDF in the radius, $F_K(R, b, c)$, as represented by Eq. (103). Table 9 shows the theoretical statistical parameters.

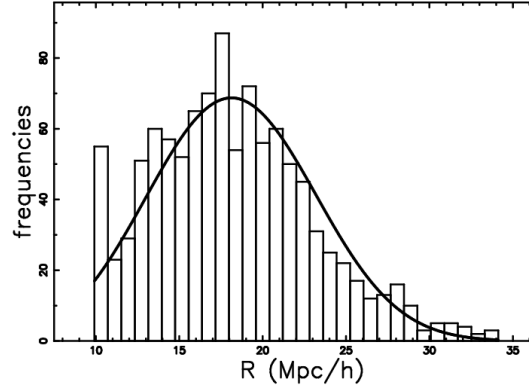


Figure 19. Histogram (step-diagram) of the effective radius in the SDSS DR7 with a superposition of the PDF in radius of the NPVT spheres, $F_K(R, b, c)$, as represented by Eq. (103). The number of bins is 30, $b=31.33$ Mpc, and $c = 1.768$.

Table 9. The statistical parameters of the theoretical radius of the NPVT spheres as represented by Eq. (103) when $b=31.33$ Mpc and $c = 1.768$.

<i>parameter</i>	<i>value</i>
<i>mean</i>	$18.23h^{-1} \text{ Mpc}$
<i>variance</i>	$23.31h^{-2} \text{ Mpc}^2$
<i>standard deviation</i>	$4.82h^{-1} \text{ Mpc}$
<i>skewness</i>	0.072
<i>kurtosis</i>	-0.162

Table 10. NPVT parameters of $f(r)_{NPVTK}$, Eq. (108).

<i>Parameter</i>	<i>value</i>
<i>Mean</i>	0.488
<i>Variance</i>	0.0323
<i>Mode</i>	0.517
<i>Skewness</i>	-0.114
<i>Kurtosis</i>	2.614

The result of the integration of the fundamental Eq. (80) inserting $c=2$ gives the following PDF for the radius of the cuts

$$f(r)_{NPVTK} = 3.4148 \sqrt[6]{3} \sqrt[3]{\pi r} 2^{2/3} G_{2,4}^{4,0} \left(\frac{16}{9} \pi^2 r^6 \middle| \begin{matrix} 1/6, 1/2 \\ 4/3, 2/3, 1/3, 0 \end{matrix} \right) \quad (107)$$

$$0 \leq r \leq 1.$$

The statistics of NPVT cuts with $c=2$ are shown in Table 10.

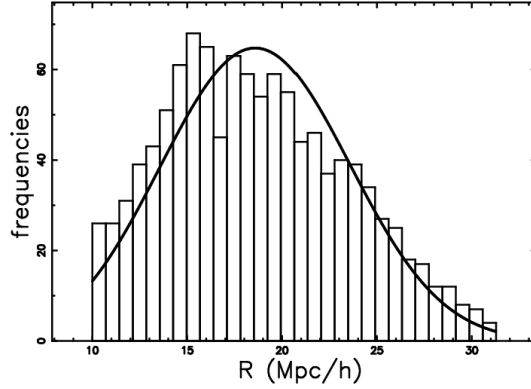


Figure 20. Histogram (step-diagram) of the simulated effective radius of SDSS DR7 with a superposition of the PDF in radius of the PVT spheres as represented by Eq. (103). The artificial sample has a minimum value of 10/h Mpc, the number of bins is 30, $b = 31.5/h$ Mpc, and $c = 1.3$.

On introducing the scaling parameter b , the PDF which describes the radius of the cut becomes

$$f(x, b)_{NPVTK} = 3.4148 \sqrt[6]{3} \sqrt[3]{\pi} x^{2/3} G_{2,4}^{4,0} \left(\frac{16}{9} \frac{\pi^2 x^6}{b^6} \middle| \begin{matrix} 1/6, 1/2 \\ 4/3, 2/3, 1/3, 0 \end{matrix} \right) \frac{1}{\sqrt[3]{\pi}} \\ 0 \leq r \leq b.$$

The SF of the *second* NPVT case, SF_{NPVTK} , with the scaling parameter b , is

$$SF(x, b)_{NPVTK} = 1 - 0.2845 \cdot 3^{5/6} \sqrt[3]{2} G_{3,5}^{4,1} \left(\frac{16}{9} \frac{\pi^2 x^6}{b^6} \middle| \begin{matrix} 1, 1/2, 5/6 \\ 5/3, 1, 2/3, 1/3, 0 \end{matrix} \right) \frac{1}{\sqrt[3]{\pi}} \\ 0 \leq r \leq b.$$

A careful exploration of the distribution in effective radius of SDSS DR7 reveals that the detected voids have radius $\geq 10/h$ Mpc. This observational fact demands the generation of random numbers in the distribution in radii of the 3D cells as given by Eq. (103) with a minimal value of 10/h Mpc. The artificial sample is generated through a numerical computation of the inverse function [89] and displayed in Fig. 20; the sample's statistics are shown in Table 11.

More details can be found in [88].

9. The cellular structure of the Universe

From a simplified point of view the galaxies belonging to a given catalog are characterized by the astronomical coordinates, the redshift and the apparent magnitude. Starting from the second CFA2 redshift Survey, the catalogs were organized in slices of a given opening angle, 3° or 6° , and a given angular extension, for example 130° . When plotted in polar coordinates of $c_l z$ the spatial distribution of galaxies is not random but distributed on filaments. Particular attention should be paid to the fact that the astronomical slices are not a plane which intersects a Voronoi Network. In order to quantify this effect we introduce a confusion distance, DV_c , as

Table 11. The statistical parameters of the artificially generated radius with a lower bound of $10/h$ Mpc, $c = 1.3$ and $b = 31.5/h$ Mpc.

<i>parameter</i>	<i>value</i>
<i>mean</i>	$18.69h^{-1} \text{ Mpc}$
<i>variance</i>	$22.74h^{-2} \text{ Mpc}^2$
<i>standard deviation</i>	$4.76h^{-1} \text{ Mpc}$
<i>skewness</i>	0.33
<i>kurtosis</i>	-0.623
<i>maximum value</i>	$31.27h^{-1} \text{ Mpc}$
<i>minimum value</i>	$10h^{-1} \text{ Mpc}$

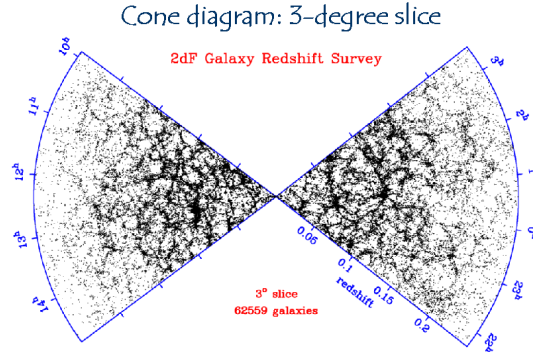


Figure 21. Slice of $75^\circ \times 3^\circ$ in the 2dFGRS. This plot contains 62559 galaxies and belongs to the 2dFGRS Image Gallery available at the web site: <http://msowwww.anu.edu.au/2dFGRS/>.

the distance after which the half altitude of the slices equalizes the observed average diameter \overline{DV}^{obs}

$$DV_c \tan(\alpha) = \frac{1}{2} \overline{DV}^{obs} \quad , \quad (110)$$

where α is the opening angle of the slice and \overline{DV}^{obs} the averaged diameter of voids. In the case of 2dFGRS $\alpha = 3^\circ$ and therefore $DV_c = 2.57 \cdot 10^4 \frac{Km}{sec}$ when $\overline{DV}^{obs} = 2700 \frac{Km}{sec}$. For values of $c_l z$ greater than DV_c the voids in the distribution of galaxies are dominated by the confusion. For values of $c_l z$ lower than DV_c the filaments of galaxies can be considered the intersection between a plane and the faces of the Voronoi Polyhedrons. A measure of the portion of the sky covered by a catalog of galaxies is the area covered by a unitarian sphere which is 4π steradians or $\frac{129600}{\pi}$ square degrees. In the case of 2dFGRS the covered area of two slices of 75° long and 3° wide, as in Fig. 21, is $\frac{1414}{\pi}$ square degrees or 0.13 sr . In the case of RC3 the covered area it is 4π steradians with the exclusion of the *Zone of Avoidance*, see Fig. 2.

In the following we will simulate the 2dFGRS, a catalog that occupies a small area of the sky, the RC3 a catalog that occupies all the sky and the CFA2 catalog.

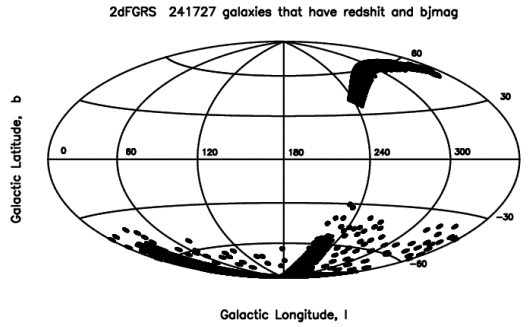


Figure 22. Hammer-Aitoff projection in galactic coordinates of 230540 galaxies in the 2dFGRS which have bJmag and redshift < 0.3 .

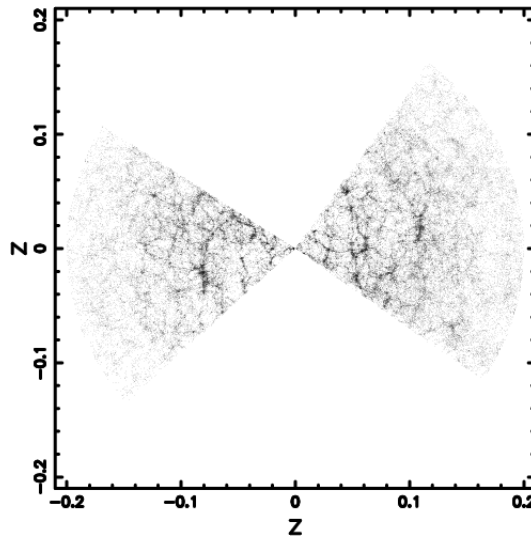


Figure 23. Cone-diagram of all the galaxies in the 2dFGRS. This plot contains 203249 galaxies.

In the case of 3C3 we demonstrate how it is possible to simulate the *Zone of Avoidance* in the theoretical simulation. The paragraph ends with a discussion on the Eridanus super-void also known as "Cold Spot".

9.1. The 2dFGRS

Fig. 22 shows the galaxies of the 2dFGRS with $z < 0.3$ in galactic coordinates and the two strips in the 2dFGRS are shown in Fig. 23.

Fig. 21 conversely reports the 2dFGRS catalog when a slice of $75^\circ \times 3^\circ$ is taken into account. This slice represents the object to simulate.

The previous observational slice can be simulated by adopting the Voronoi network reported in Fig. 11.

The distribution of the galaxies as given by the Voronoi Diagrams is reported in Fig. 24 where all the galaxies are considered. In this case the galaxies are

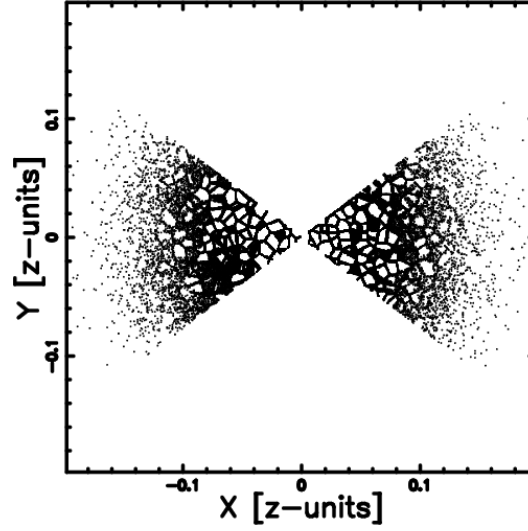


Figure 24. Polar plot of the pixels belonging to a slice 75° long and 3° wide. This plot contains 62563 galaxies, the maximum in the frequencies of theoretical galaxies is at $z = 0.043$. In this plot $\mathcal{M}_\odot = 5.33$ and $h=0.623$.

Table 12. Real and Simulated data of the slice 75° long and 3° wide .

	<i>2dFGRS</i>	<i>simulation</i>
<i>elements</i>	62559	62563
z_{min}	0.001	0.011
$z_{pos-max}$	0.029	0.042
z_{ave}	0.051	0.058
z_{max}	0.2	0.2

extracted according to the integral of the Schechter function in flux (formula (15) with parameters as in Table 2). Table 12 reports the basic data of the astronomical and simulated data of the $75^\circ \times 3^\circ$ slice.

When conversely a given interval in flux (magnitudes) characterized by f_{min} and f_{max} is considered the number of galaxies, N_{SC} , of a 3° slice can be found with the following formula

$$N_{SC} = N_C \frac{\int_{f_{min}}^{f_{max}} 4\pi \left(\frac{c_l}{H_0}\right)^5 z^4 \Phi\left(\frac{z^2}{z_{crit}^2}\right) df}{\int_{f_{min,C}}^{f_{max,C}} 4\pi \left(\frac{c_l}{H_0}\right)^5 z^4 \Phi\left(\frac{z^2}{z_{crit}^2}\right) df}, \quad (111)$$

where $f_{min,C}$ and $f_{max,C}$ represent the minimum and maximum flux of the considered catalog and N_C all the galaxies of the considered catalog; a typical example is reported in Fig. 25.

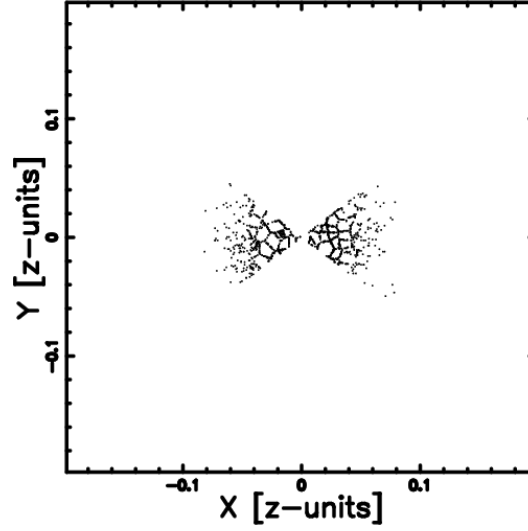


Figure 25. Polar plot of the pixels belonging to a slice 75° long and 3° wide. Galaxies with magnitude $15.02 \leq bJmag \leq 15.31$ or $46767 \frac{L_\odot}{Mpc^2} \leq f61063 \frac{L_\odot}{Mpc^2}$. The maximum in the frequencies of theoretical galaxies is at $z = 0.029$, $N_{SC}=2186$ and $N_C=62559$. In this plot $M_\odot = 5.33$ and $h=0.623$.

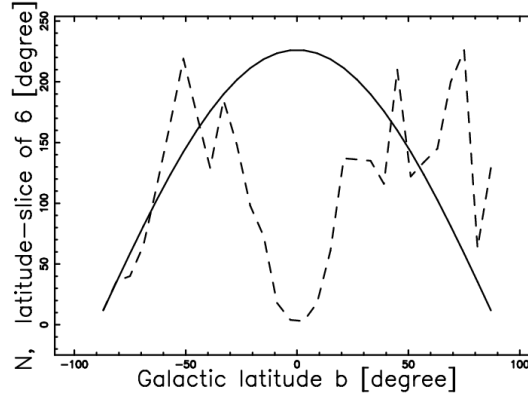


Figure 26. The galaxies in the RC3 which have BT and redshift are organized in frequencies versus galactic latitude b (dashed line). The theoretical fit represents N_i (full line).

9.2. The Third Reference Catalog of Bright Galaxies

We now test the concept of an isotropic universe. This can be done by plotting the number of galaxies comprised in a slice of 360° in galactic longitude versus a variable number Δb in galactic latitude, for example 6° . The number of galaxies in the RC3 versus galactic latitude is plotted in Fig. 26.

The solid angle $d\Omega$ in spherical coordinates (r, θ, ϕ) is

$$d\Omega = \sin(\theta)d\theta d\phi \quad . \quad (112)$$

Table 13. Real and Simulated data without the *Zone of Avoidance* in the RC3 catalog.

	RC3	no ZOA
<i>elements</i>	3316	4326
z_{min}	5.7×10^{-7}	8.9×10^{-3}
$z_{pos-max}$	5.6×10^{-3}	8.9×10^{-2}
z_{ave}	1.52×10^{-2}	7.96×10^{-2}
z_{max}	9.4×10^{-2}	0.14

In a slice of $360^\circ \times \Delta b$ the amount of solid angle, $\Delta\Omega$, is

$$\Delta\Omega = 2\pi((\cos(90^\circ) - \cos(b + \Delta b)) - (\cos(90^\circ) - \cos(b))) \text{ steradians} \quad (113)$$

The approximate number of galaxies in each slice can be found through the following approximation. Firstly, we find the largest value of the frequencies of galaxies, F_i , versus b , $max(F_i)$ where the index i denotes a class in latitude. We therefore find the largest value of $\Delta\Omega_i$, $max(\Delta\Omega_i)$. The introduction of the multiplicative factor M

$$M = \frac{max(F_i)}{max(\Delta\Omega_i)} \quad , \quad (114)$$

obtains the following theoretical evaluation of the number of galaxies N_i as a function of the latitude,

$$N_i = M \times \Delta\Omega_i \quad . \quad (115)$$

This number, N_i , as a function of b is plotted in Fig. 26.

The simulation of this overall sky survey can be done in the following way:

- The pixels belonging to the faces of irregular polyhedron are selected according to the distribution in z of the galaxies in the RC3 catalog which have redshift and BT.
- A second operation selects the pixels according to the distribution in latitude in the RC3 catalog, see Fig. 27.
- In order to simulate a theoretical distribution of objects which represent the RC3 catalog without the *Zone of Avoidance* we made a series of 6° slices in latitude in the RC3 catalog, selecting N_i pixels in each slice, see Fig. 28. In order to ensure that the range in z is correctly described Table 13 reports z_{min} , $z_{pos-max}$, z_{ave} and z_{max} which represent the minimum z , the position in z of the maximum in the number of galaxies, and the maximum z in the RC3 catalog or the simulated sample.

9.3. The CFA2 catalog

The results of the simulation can be represented by a slice similar to that observed (a strip of 6° wide and about 130° long) , see Fig. 29.

A typical polar plot once the "scaling" algorithm is implemented , see [35] , is reported in Fig. 30; it should be compared with the observations , see Fig. 31.

Fig. 32 reports both the CFA2 slice as well the simulated slice.

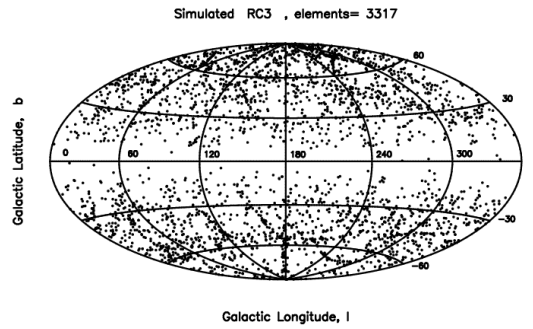


Figure 27. Hammer-Aitoff projection of 3317 pixels belonging to a face of an irregular Voronoi Polyhedron. The *Zone of Avoidance* at the galactic plane follows Fig. 2. This plot simulates the RC3 galaxies which have BT and redshift. The galaxies are extracted according to the integral of the Schechter function in flux (formula (15) with parameters as in Table 2)

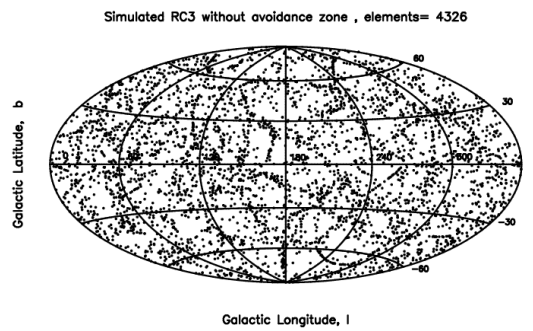


Figure 28. Hammer-Aitoff projection of 4326 pixels belonging to a face of an irregular Voronoi Polyhedron. This plot simulates the RC3 galaxies which have BT and redshift but the *Zone of Avoidance* at the galactic plane is absent. The galaxies are extracted according to the integral of the Schechter function in flux (formula (15) with parameters as in Table 2)

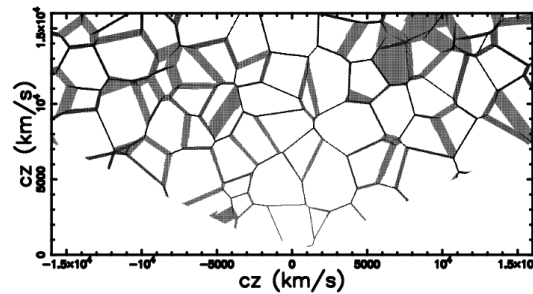


Figure 29. Polar plot of the little cubes belonging to a slice 130° long and 6° wide.

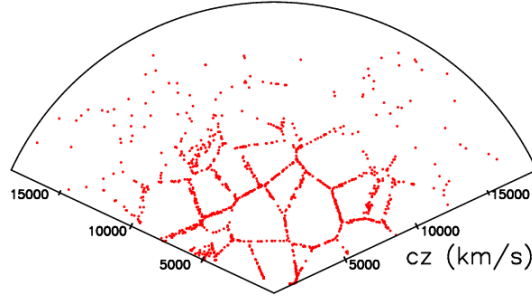


Figure 30. Polar plot of the little cubes (red points) when the "scaling" algorithm is applied. Parameters as in Fig. 29 . This plot simulates the CFA2 slice.

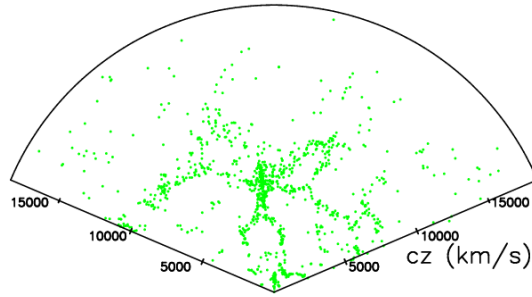


Figure 31. Polar plot of the real galaxies (green points) belonging to the second CFA2 redshift catalog.

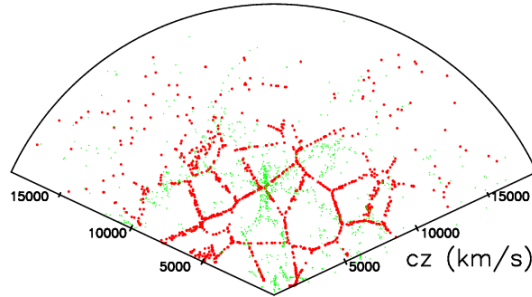


Figure 32. Polar plot of the real galaxies (green points) belonging to the second CFA2 redshift catalog and the little cubes (red points).

9.4. The Eridanus Supervoid

A void can be defined as the empty space between filaments in a slice and the typical diameter has a range of $[11 - 50] Mpc/h$, see [90] and [91]. The probability, for example, of having a volume 3 times bigger than the average is $3.2 \cdot 10^{-3}$ for PDF (55) when $d = 3$ and $2.1 \cdot 10^{-3}$ for PDF (47) when $d = 2.75$. Particularly large voids are called super-voids and have a range of $[110 - 163] Mpc/h$.

Special attention should be paid to the Eridanus super-void of $300 Mpc$ in

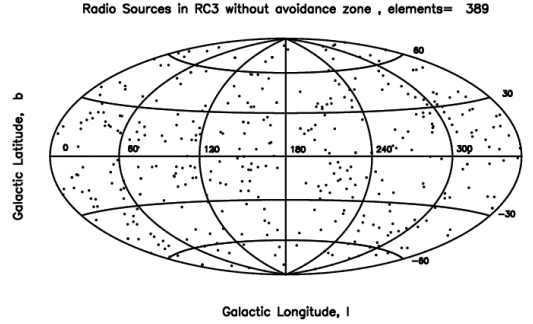


Figure 33. Hammer-Aitoff projection of the SDSS-FIRST sources with complex radio morphology belonging to the RC3, $p_{rs} = 0.09$. Other parameters as in Fig. 28.

diameter. This super-void was detected by the Wilkinson Microwave Anisotropy Probe (WMAP), see [92, 93, 94] and was named *Cold Spot*. The WMAP measures the temperature fluctuations of the cosmic microwave background (CMB). Later on the astronomers confirmed the largest void due to the fact that the density of radio sources at 1.4 GHz is anomalously low in the direction of the *Cold Spot*, see [95] and [96]. The standard statistics of the Voronoi normalized volume distribution in 3D covers the range [0.1 – 10]. In the case of a Eridanus super-void the normalized volume is $\approx \frac{300}{27} = 1.37 \cdot 10^3$ and the connected probability of having such a super-void is $1.47 \cdot 10^{-18}$ when the Ferenc & Neda function with $d = 3$, formula (55), is used and ≈ 0 when the Kiang function with $d = 2.75$, formula (47) is used.

Due to this low probability of having such a large normalized volume we mapped a possible spatial distribution of the SDSS-FIRST (the Faint Images of the Radio Sky at Twenty cm survey) sources with complex radio morphology from the theoretical distribution of galaxies belonging to the RC3. The fraction of galaxies belonging to the 2dFGRS detected as SDSS-FIRST sources with complex radio morphology is less than 10% according to Section 3.8 in [97]. We therefore introduced a probability, p_{rs} , that a galaxy is a radio source. The number of SDSS-FIRST sources N_{rs} in the RC3 which are SDSS-FIRST sources with complex radio morphology is

$$N_{rs} = p_{rs} * N_g \quad , \quad (116)$$

where N_g is the number of galaxies in the theoretical RC3.

From a visual inspection of Fig. 28 and Fig. 33 it is possible to conclude that the voids increase in size when radiogalaxies which are a subset of the galaxies are considered.

10. The correlation function for galaxies

Galaxies have the tendency to be grouped in clusters and a typical measure is the computation of the two-points correlation function for galaxies, see [98, 6]. The correlation function can be computed in two ways: a local analysis in the range $[0 - 16]Mpc/h$ and an extended analysis in the range $[0 - 200]Mpc/h$.

10.1. The local analysis

A first way to describe the degree of clustering of galaxies is the two point correlation function $\xi_{GG}(r)$, usually presented in the form

$$\xi_{GG} = \left(\frac{r}{r_G}\right)^{-\gamma_{GG}} \quad , \quad (117)$$

where $\gamma_{GG}=1.8$ and $r_G = 5.77h^{-1}Mpc$ (the correlation length) when the range $0.1h^{-1}Mpc < r < 16h^{-1}Mpc$ is considered, see [99] where 118149 galaxies were analyzed.

In order to compute the correlation function, two volumes were compared: one containing the little cubes belonging to a face, the other containing a random distribution of points. From an analysis of the distances of pairs, the minimum and maximum were computed and $n_{DD}(r)$ was obtained, where $n_{DD}(r)$ is the number of pairs of galaxies with separation within the interval $[r - dr/2, r + dr/2]$. A similar procedure was applied to the random elements in the same volume with the same number of elements and $n_{RR}(r)$ is the number of pairs of the Poissonian Process. According to formula (16.4.6) in [100] the correlation function is:

$$\xi_{GG}(r) = \frac{n_{DD}(r)}{n_{RR}(r)} - 1 \quad . \quad (118)$$

To check whether ξ_{GG} obeys a power law or not we used a simple linear regression test with the formula:

$$\text{Log } \xi_{GG} = a + b \text{ Log } r \quad , \quad (119)$$

which allows us to compute $r_G = 10^{-a/b}$ and $\gamma_{GG}=-b$.

We now outline the method that allow us to compute the correlation function using the concept of thick faces, see [101]. A practical implementation is to consider a decreasing probability of having a galaxy in the direction perpendicular to the face. As an example we assume a probability, $p(x)$, of having a galaxy outside the face distributed as a Normal (Gaussian) distribution

$$p(x) = \frac{1}{\sigma(2\pi)^{1/2}} \exp -\frac{x^2}{2\sigma^2} \quad , \quad (120)$$

where x is the distance in Mpc from the face and σ the standard deviation in Mpc . Once the complex 3D behavior of the faces of the Voronoi Polyhedron is set up we can memorize such a probability on a 3D grid $P(i, j, k)$ which can be found in the following way

- In each lattice point (i, j, k) we search for the nearest element belonging to a Voronoi face. The probability of having a galaxy is therefore computed according to formula (120).
- A number of galaxies, $N_G = n_* \times side^3$ is then inserted in the box; here n_* represents the density of galaxies

Fig. 34 visualizes the edges belonging to the Voronoi diagrams and Fig. 35 represents a cut in the middle of the probability, $P(i, j, k)$, of having a galaxy to a given distance from a face.

A typical result of the simulation is reported in Fig. 36 where the center of the smaller box in which the correlation function is computed is the point belonging to a face nearest to the center of the big box.

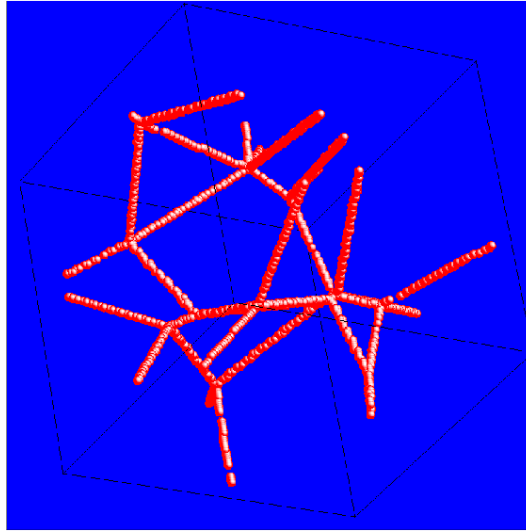


Figure 34. 3D visualization of the edges of the Poissonian Voronoi-diagram. The parameters are $pixels=60$, $N_s=12$, $side=96.24\text{ Mpc}$, $h=0.623$ and $amplify=1.2$.

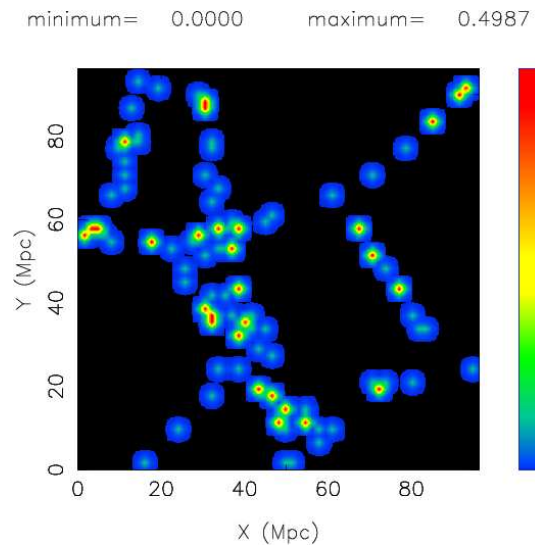


Figure 35. Cut in the middle of the 3D grid $P(i, j, k)$ which represents a theoretical 2D map of the probability of having a galaxy. The Voronoi parameters are the same as in Fig. 34 and $\sigma=0.8\text{ Mpc}$. The X and Y units are in Mpc.

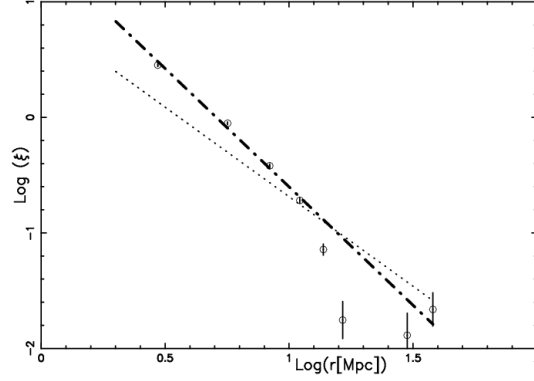


Figure 36. The logarithm of the correlation function is visualized through points with their uncertainty (vertical bar), the asymptotic behavior of the correlation function ξ_{GG} is reported as dash-dot-dash line; in our simulation $\gamma_{GG}=2.04$ and $r_G = 5.08$ Mpc. The standard value of the correlation function is reported as a dotted line; from the point of view of the observations in average $\gamma_{GG}=1.8$ and $r_G = 5$ Mpc. Parameters of the simulation as in Fig. 34.

From an analysis of Fig. 36 we can deduce that the correlation function ξ_{GG} of the simulation has a behavior similar to the standard one. Perhaps the value r_G is a simple measure of the face's thickness, ΔR_F . From this point of view on adopting a standard value of the expanding shell thickness, $\Delta R = \frac{R}{12}$ and assuming that the thickness of the shell is made by the superposition of two expanding shells the following is obtained

$$\Delta R_F \approx \frac{R}{6} \approx \frac{D^{obs}}{h \cdot 12} = 3.62 \text{ Mpc} \quad , \quad (121)$$

where $h = 0.623$ has been used. The correlation dimension D_2 , see [1], is connected with the exponent γ through the relation:

$$D_2 = 3 - \gamma \quad . \quad (122)$$

Here there is the case in which the mass $M(r)$ increases as $r^{1.2}$, in the middle of a one dimensional structure ($M(r) \propto r$) and a two dimensional sheet ($M(r) \propto r^2$), see [100]. In this paragraph the dependence of the correlation function on the magnitude is not considered.

10.2. The extended analysis

A second definition of the correlation function takes account of the Landy-Szalay border correction, see [102],

$$\xi_{LS}(s) = 1 + \frac{n_{DD}(s)}{n_{RR}(s)} - 2 \frac{n_{DR}(s)}{n_{RR}(s)} \quad . \quad (123)$$

where $n_{DD}(s)$, $n_{DD}(s)$ and $n_{DR}(s)$ are the number of galaxy-galaxy, random-random and galaxy-random pairs having distance s , see [103]. A random catalog of galaxies in polar coordinates can be built by generating a first random number $\propto z^2$ in the z -space and a second random angle in the interval $[0, 75]$. A test of our code for the correlation function versus a more sophisticated code is reported in Fig. 37 for

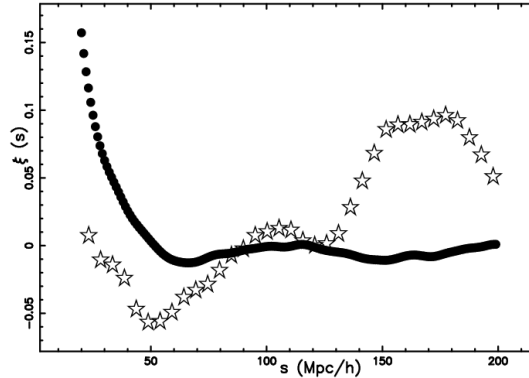


Figure 37. Redshift-space correlation function for the 2dFGRS sample limited at $z = 0.12$ as given by our code (empty stars) and the results of [103] (full points) for 2dFVL. The covered range is $[40 - 200]Mpc/h$.

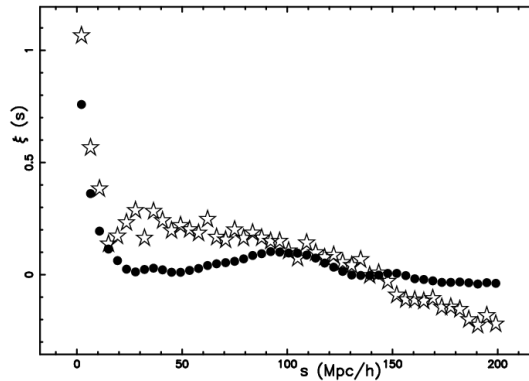


Figure 38. Redshift-space correlation function for the 2dFGRS sample (empty stars) and the Voronoi sample(full points). The covered range is $[40-200]Mpc/h$.

the 2dFVL volume limited (VL) sample, where the data available at the Web site <http://www.uv.es/martinez/> have been processed.

The pair correlation function for the vertexes of the Poissonian Voronoi Polyhedron presents a typical damped oscillation, see Figure 5.4.11 in [104], Figure 2 in [103] and Figure 3 in [105]. Here conversely : (a) we first consider a set of objects belonging to the faces of the irregular Polyhedron ; (b) we extract from the previous set a subset which follows the photometric law and then we compute the pair correlation function. The difference between our model and the model in [103] for 2dFVL can be due to the luminosity color segregation presents in 2dFVL but not in our Voronoi type model. A typical result is reported in Fig. 38 where it is possible to find the correlation function of 2dFGRS with astronomical data as reported in Fig. 23 as well as the correlation function of the Voronoi network with simulated data as reported in Fig. 24.

A careful analysis of Fig. 38 allows us to conclude that the behavior of the correlation function is similar for the astronomical data as well as the simulated

Voronoi-data. The oscillations after 100 Mpc are classified as acoustic, [106].

11. Conclusions

Photometric maximum

The observed number of galaxies in a given solid angle with a chosen flux/magnitude versus the redshift presents a maximum that is a function of the flux/magnitude. From a theoretical point of view, the photometric properties of the galaxies depend on the chosen law for the LF . The three LF s here adopted predict a maximum in the theoretical number of galaxies as a function of the redshift once the apparent flux/magnitude is fixed, for the Schechter LF see formula(13), for the $\mathcal{M} - L$ LF see formula(20) and for the generalized gamma LF see formula(30).

The theoretical fit representing the number of galaxies as a function of the redshift can be compared with the real number of galaxies of the 2dFGRS which is theory-independent. The superposition of theoretical and observed fit is acceptable, see Fig. 6. Particular attention should be paid to the Malmquist bias and to equation (37) that regulate the upper value of the redshift that defines the complete sample.

3D Voronoi Diagrams The intersection between a plane and the 3D Voronoi faces is well known as $V_p(2,3)$. The intersection between a slice of a given opening angle, for example 3° , and the 3D Voronoi faces is less known and has been developed in Section 6.2. This intersection can be calibrated on the astronomical data once the number of Poissonian seeds is such that the largest observed void matches the largest Voronoi volume. Here the largest observed void is 2700 Km/sec and in order to simulate, for example, the 2dFGRS, 137998 Poissonian seeds were inserted in a volume of $(131908 Km/sec)^3$. The intersection between a sphere and the 3D Voronoi faces represents a new way to visualize the voids in the distribution of galaxies, see Section 6.2. In this spherical cut the intersection between a sphere and the 3D Voronoi faces is no longer represented by straight lines but by curved lines presenting in some cases a cusp behavior at the intersection, see Fig. 12. In line of principle the spatial distribution of galaxies at a given redshift should follow such curved lines.

Statistics of the voids The statistical properties of the voids between galaxies can be well described by the volume distribution of the Voronoi Polyhedra. Here two distributions of probability were carefully compared: the old Kiang function here parametrized as a function of the dimension d , see formula (44), and the new distribution of Ferenc & Neda, see formula (55), which is a function of the selected dimension d . The analysis of the normalized areas of $V_p(2,3)$ is a subject of research rather than a well-established fact and we have fitted them with the Kiang function and the exponential distribution. The χ^2 value indicates that the exponential distribution fits more closely the normalized area distribution of $V_p(2,3)$ than does the Kiang function, see Table 4. This fact follows from the comparison between the exponential and Kiang distributions of the radius, see Fig. 14. Therefore, the one parameter survival function of the radius of the exponential distribution for $V_p(2,3)$, S_{ER23} , as represented by (78), may model the voids between galaxies.

Simulations of the catalogs of galaxies By combining the photometric dependence in the number of galaxies as a function of the redshift with the intersection between a slice and the Voronoi faces, it is possible to simulate the astronomical catalogs such as the 2dFGRS, see Section 9.1. Other catalogs such as the RC3 which covers all the sky (except the Zone of Avoidance) can be simulated through a given number of spherical cuts, for example 25, with progressive increasing redshift. This simulation is

visible in Fig. 27 in which the theoretical influence of the Zone of Avoidance has been inserted, and in Fig. 28 in which the theoretical RC3 without the Zone of Avoidance has been modeled. Fig. 33 reports the subset of the galaxies which are radiogalaxies.

Correlation function The standard behavior of the correlation function for galaxies in the short range $[0 - 10 \text{ Mpc}/h]$ can be simulated once 12 Poissonian seeds are inserted in a box of volume $(96.24 \text{ Mpc}/h)^3$. In this case the model can be refined by introducing the concept of galaxies generated in a thick face belonging to the Voronoi Polyhedron. The behavior of the correlation function in the large range $[40 - 200 \text{ Mpc}/h]$ of the Voronoi simulations of the 2dFGRS presents minimum variations from the processed astronomical data, see Fig. 38. We now extract a question from the conclusions of [103] “Third, the minimum in the large-distance correlation functions of some samples demands explanation: is it really the signature of voids?” Our answer is “yes”. The minimum in the large scale correlation function is due to the combined effect of the large empty space between galaxies (the voids) and to the photometric behavior of the number of galaxies as a function of the red-shift.

Stereological approach In this review analytical formulas have been provided which model the distributions of the lengths and areas of the planar sections of three-dimensional Poisson Voronoi diagrams: in particular, it has been shown that they are related to the Meier G function. This finding is consistent with the analytical results presented in [107], where it is proved that nonlinear combinations of gamma variables, such as products or quotients, have distributions proportional, or closely related, to the Meijer G distribution. The analytical distributions F_r and F_A been compared with results of numerical simulations.

Acknowledgements. I thank the 2dF Galaxy Redshift Survey team for the use of Fig. 21, which is taken from the image gallery on the 2dFGRS website (see <http://www2.aao.gov.au/2dFGRS>) and the Stanford Encyclopedia of Philosophy for the use of Fig. 1.

REFERENCES

- [1] Jones BJ, Martínez VJ, Saar E, Trimble V. Scaling laws in the distribution of galaxies. *Rev. Mod. Phys.* . 2005;76:1211–1266.
- [2] Sparke LS, Gallagher JS. *Galaxies in the universe : an introduction.* Cambridge, UK: Cambridge University Press; 2000.
- [3] Mandelbrot B. On a decomposable model of a hierarchical universe - Derivation of galactic correlations on the celestial sphere. *Academie des Sciences Paris Comptes Rendus Serie Sciences Mathematiques.* 1975;280:1551–1554.
- [4] Soneira RM, Peebles PJE. Is there evidence for a spatially homogeneous population of field galaxies. *ApJ* . 1977;211:1–15.
- [5] Soneira RM, Peebles PJE. A computer model universe - Simulation of the nature of the galaxy distribution in the Lick catalog. *AJ* . 1978;83:845–849.
- [6] Peebles PJE. *The large-scale structure of the universe.* Princeton, N.J.: Princeton University Press; 1980.
- [7] Charlton JC, Schramm DN. Percolation of explosive galaxy formation. *ApJ* . 1986;310:26–39.
- [8] Zaninetti L, Ferraro M. Transient phenomena and cluster formation. *A&A* . 1990;239:1–2.
- [9] Klypin A, Shandarin SF. Percolation technique for galaxy clustering. *ApJ* . 1993;413:48–58.
- [10] Berlind AA, Frieman J, Weinberg DH, et al . Percolation Galaxy Groups and Clusters in the SDSS Redshift Survey: Identification, Catalogs, and the Multiplicity Function. *ApJS* . 2006;167:1–25.
- [11] Vogeley MS, Geller MJ, Huchra JP. Void statistics of the CfA redshift survey. *ApJ* . 1991;382:44–54.
- [12] Vogeley MS, Geller MJ, Park C, Huchra JP. Voids and constraints on nonlinear clustering of galaxies. *AJ* . 1994;108:745–758.
- [13] Hoyle F, Vogeley MS. Voids in the Point Source Catalogue Survey and the Updated Zwicky Catalog. *ApJ* . 2002;566:641–651.

- [14] Pan DC, Vogeley MS, Hoyle F, Choi YY, Park C. Cosmic Voids in Sloan Digital Sky Survey Data Release 7. ArXiv e-prints:11034156. 2011;.
- [15] Voronoi GF. Nouvelles applications des parametres continus a la theorie des formes quadratique, Premier Memoire : Sur quelques proprietes des formes quadratiques ... Z. *Reine Angew Math.* 1907;133:97–178.
- [16] Voronoi GF. Nouvelles applications des parametres continus a la theorie des formes quadratique, Deuxieme Memoire : Recherches sur les Paralleloedres Primitifs. *Z. Reine Angew Math.* 1908;134:198–287.
- [17] Descartes R. *Principia Philosophiae*. Amsterdam: Ludovicus Elzevirius; 1644.
- [18] Aurenhammer, F and Klein, R In : Sack, J -R , editor. *Voronoi diagrams*. Amsterdam: North-Holland; 2000.
- [19] Kiang T. Random Fragmentation in Two and Three Dimensions. *Z. Astrophys.* . 1966;64:433–439.
- [20] Icke V, van de Weygaert R. Fragmenting the universe. *A&A* . 1987;184:16–32.
- [21] van de Weygaert R, Icke V. Fragmenting the universe. II - Voronoi vertices as Abell clusters. *A&A* . 1989;213:1–2.
- [22] Pierre M. Probes for the large-scale structure. *A&A* . 1990;229:7–16.
- [23] Barrow JD, Coles P. The statistics of primordial density fluctuations. *MNRAS* . 1990;244:188–192.
- [24] Coles P, Barrow JD. Microwave background constraints on the Voronoi model of large-scale structure. *MNRAS* . 1990;244:557–562.
- [25] Coles P. Understanding recent observations of the large-scale structure of the universe. *Nature* . 1990;346:446.
- [26] van de Weygaert R. Quasi-periodicity in deep redshift surveys. *MNRAS* . 1991;249:159–163.
- [27] van de Weygaert R. Voids and the large scale structure of the universe. PhD thesis, University of Leiden. 1991;.
- [28] Zaninetti L. Dynamical Voronoi tessellation. III - The distribution of galaxies. *A&A* . 1991;246:291–300.
- [29] Ikeuchi S, Turner EL. Quasi-periodic structures in the large-scale galaxy distribution and three-dimensional Voronoi tessellation. *MNRAS* . 1991;250:519–522.
- [30] Subba Rao MU, Szalay AS. Statistics of pencil beams in Voronoi foams. *ApJ* . 1992;391:483–493.
- [31] van de Weygaert R. Fragmenting the Universe. 3: The constructions and statistics of 3-D Voronoi tessellations. *A&A* . 1994;283:361–406.
- [32] Goldwirth DS, da Costa LN, van de Weygaert R. The Two-Point Correlation Function and the Size of Voids. *MNRAS* . 1995;275:1185–1195.
- [33] van de Weygaert R. Froth across the Universe Dynamics and Stochastic Geometry of the Cosmic Foam. arXiv:astro-ph/0206427. 2002;.
- [34] van de Weygaert R. In: *Statistics of Galaxy Clustering - Commentary*. Statistical Challenges in Astronomy; 2003. p. 156–186.
- [35] Zaninetti L. On the Large-Scale Structure of the Universe as given by the Voronoi Diagrams. *Chinese J. Astron. Astrophys.* . 2006;6:387–395.
- [36] Ebeling H, Wiedenmann G. Detecting structure in two dimensions combining Voronoi tessellation and percolation. *Phys. Rev. E* . 1993;47:704–710.
- [37] Bernardeau F, van de Weygaert R. A new method for accurate estimation of velocity field statistics. *MNRAS* . 1996;279:693–701.
- [38] Schaap WE, van de Weygaert R. Continuous fields and discrete samples: reconstruction through Delaunay tessellations. *A&A* . 2000;363:L29–L32.
- [39] Marinoni C, Davis M, Newman JA, Coil AL. Three-dimensional Identification and Reconstruction of Galaxy Systems within Flux-limited Redshift Surveys. *ApJ* . 2002;580:122–143.
- [40] Melnyk OV, Elyiv AA, Vavilova IB. The structure of the local supercluster of galaxies detected by three-dimensional Voronoi's tessellation method. *Kinematika i Fizika Nebesnykh Tel.* 2006;22:283–296.
- [41] van de Weygaert R, Schaap W. The Cosmic Web: Geometric Analysis. In: V J Martinez, E Saar, E M Gonzales, & M J Pons-Borderia , editor. *Lecture Notes in Physics*, Berlin Springer Verlag. vol. 665 of *Lecture Notes in Physics*, Berlin Springer Verlag; 2009. p. 291–311.
- [42] Elyiv A, Melnyk O, Vavilova I. High-order 3D Voronoi tessellation for identifying isolated galaxies, pairs and triplets. *MNRAS* . 2009;394:1409–1418.
- [43] Aarseth SJ. Computer simulations of galaxy clustering. In: *The large scale structure of the*

- universe, p. 189 - 196; 1978. p. 189–196.
- [44] Turner EL, Aarseth SJ, Blanchard NT, Mathieu RD, Gott JR III. N-body simulations of galaxy clustering. II - Groups of galaxies. *ApJ* . 1979;228:684–695.
- [45] Gott JR III, Turner EL, Aarseth SJ. N-body simulations of galaxy clustering. III - The covariance function. *ApJ* . 1979;234:13–26.
- [46] Evrard AE, MacFarland TJ, Couchman HMP, Colberg JM, Yoshida N, White SDM, et al. Galaxy Clusters in Hubble Volume Simulations: Cosmological Constraints from Sky Survey Populations. *ApJ* . 2002;573:7–36.
- [47] Peebles PJE. A model for continuous clustering in the large-scale distribution of matter. *Astrophysics and Space Science* . 1974;31:403–410.
- [48] Peebles PJE. The Gravitational-Instability Picture and the Nature of the Distribution of Galaxies. *ApJ* . 1974;189:51–59.
- [49] Gott JR III, Rees MJ. A theory of galaxy formation and clustering. *A&A* . 1975;45:365–376.
- [50] Zel'dovich YB. Gravitational instability: An approximate theory for large density perturbations. *A&A* . 1970;5:84–89.
- [51] Shandarin SF, Zel'dovich YB. The large-scale structure of the universe: Turbulence, intermittency, structures in a self-gravitating medium. *Rev. Mod. Phys.* . 1989;61:185–220.
- [52] Sahni V, Coles P. Approximation methods for non-linear gravitational clustering. *Phys. Rep.* . 1995;262:1–135.
- [53] Neyman J, Scott EL. A Theory of the Spatial Distribution of Galaxies. *ApJ* . 1952;116:144–154.
- [54] Scherrer RJ, Bertschinger E. Statistics of primordial density perturbations from discrete seed masses. *ApJ* . 1991;381:349–360.
- [55] Cooray A, Sheth R. Halo models of large scale structure. *Phys. Rep.* . 2002;372:1–129.
- [56] Hubble E. A Relation between Distance and Radial Velocity among Extra-Galactic Nebulae. *Proceedings of the National Academy of Science*. 1929;15:168–173.
- [57] Sandage A, Tammann GA, Saha A, Reindl B, Macchetto FD, Panagia N. The Hubble Constant: A Summary of the Hubble Space Telescope Program for the Luminosity Calibration of Type Ia Supernovae by Means of Cepheids. *ApJ* . 2006;653:843–860.
- [58] Mattig W. Über den Zusammenhang zwischen Rotverschiebung und scheinbarer Helligkeit. *Astronomische Nachrichten*. 1958;284:109–119.
- [59] Lang KR. *Astrophysical formulae*. (Third Edition). New York: Springer; 1999.
- [60] Schechter P. An analytic expression for the luminosity function for galaxies. *ApJ* . 1976;203:297–306.
- [61] Padmanabhan T. *Cosmology and Astrophysics through Problems*. Cambridge: Cambridge University Press; 1996.
- [62] Padmanabhan P. *Theoretical astrophysics. Vol. III: Galaxies and Cosmology*. Cambridge, MA: Cambridge University Press; 2002.
- [63] Zaninetti L. A new luminosity function for galaxies as given by the mass-luminosity relationship . *AJ* . 2008;135:1264–1275.
- [64] Evans M, Hastings N, Peacock B. *Statistical Distributions - third edition*. New York: John Wiley & Sons Inc; 2000.
- [65] Zaninetti L. The Luminosity Function of Galaxies as modelled by the Generalized Gamma Distribution . *Acta Physica Polonica B*. 2010;41(4):729–751.
- [66] de Vaucouleurs G, de Vaucouleurs A, Corwin HG Jr, Buta RJ, Paturel G, Fouque P. *Third Reference Catalogue of Bright Galaxies*. New York, NY: Springer-Verlag; 1991.
- [67] Jarrett T. Large Scale Structure in the Local Universe - The 2MASS Galaxy Catalog. *PASA* . 2004;21:396–403.
- [68] Crook AC, Huchra JP, Martimbeau N, Masters KL, Jarrett T, Macri LM. Groups of Galaxies in the Two Micron All Sky Redshift Survey. *ApJ* . 2007;655:790–813.
- [69] Geller MJ, Huchra JP. Mapping the universe. *Science*. 1989;246:897–903.
- [70] Malmquist KG. A study of the stars of spectral type A . *Lund Medd Ser II*. 1920;22:1–10.
- [71] Malmquist KG. On some relations in stellar statistics . *Lund Medd Ser I*. 1922;100:1–10.
- [72] Behr A. Zur Entfernungsskala der extragalaktischen Nebel. *Astronomische Nachrichten*. 1951;279:97–107.
- [73] Zaninetti L. A geometrical model for the catalogs of galaxies . *Revista Mexicana de Astronomia y Astrofisica*. 2010;46:115–134.
- [74] Neyrinck MC, Gnedin NY, Hamilton AJS. VOBOZ: an almost-parameter-free halo-finding algorithm. *MNRAS* . 2005;356:1222–1232.
- [75] Press WH, Teukolsky SA, Vetterling WT, Flannery BP. *Numerical Recipes in FORTRAN. The Art of Scientific Computing*. Cambridge: Cambridge University Press; 1992.

- [76] Hinde AL, Miles RE. Monte Carlo estimates of the distributions of the random polygons of the Voronoi tessellation with respect to a Poisson process. *J Stat Comput Simul.* 1980;10:205–223.
- [77] Ferenc JS, Nédá Z. On the size distribution of Poisson Voronoi cells. *Phys. A.* 2007;385:518–526.
- [78] Tanemura M. Statistical Distributions of Poisson Voronoi Cells in Two and Three Dimensions. *Forma.* 2003;18:221–247.
- [79] Zaninetti L. Practical Statistics for the Voids Between Galaxies. *Serbian Astronomical Journal.* 2010;181:19–29.
- [80] Møller J. Random tessellations in $R^* * d$. *Adv Appl Probab.* 1989;21(1):37–73.
- [81] Møller J. Lectures on random Voronoi tessellations. *Lecture Notes in Statistics* (Springer). 87. New York, NY: Springer-Verlag. 134 p. DM 49.00; öS 382.20; sFr. 49.00 ; 1994.
- [82] Chiu SN, Weygaert RVD, Stoyan D. The Sectional Poisson Voronoi Tessellation Is Not a Voronoi Tessellation. *Advances in Applied Probability.* 1996;28(2):356–376.
- [83] Blower JD, Keating JP, Mader HM, Phillips JC. The evolution of bubble size distributions in volcanic eruptions. *Journal of Volcanology and Geothermal Research.* 2002;120(1-2):1 – 23.
- [84] Ferraro M, Zaninetti L. Statistics of cross sections of Voronoi tessellations. *Phys. Rev. E.* 2011;84(4):041107.
- [85] Meijer CS. Über Whittakersche bzw. Besselsche Funktionen und deren Produkte. *Nieuw Arch Wiskd.* 1936;18:10–39.
- [86] Meijer CS. Multiplikationstheoreme für die Funktion $C_{p,q}^{m,n}(z)$. *Proc Akad Wet Amsterdam.* 1941;44:1062–1070.
- [87] Olver FWJ, Lozier DWE, Boisvert RFe, Clark CWe. *NIST handbook of mathematical functions.* Cambridge: Cambridge University Press. ; 2010.
- [88] Zaninetti L. New Analytical Results for Poissonian and non-Poissonian Statistics of Cosmic Voids. *Revista Mexicana de Astronomia y Astrofisica.* 2012;48:209–222.
- [89] Brandt S, Gowan G. *Data Analysis: Statistical and Computational Methods for Scientists and Engineers.* New-York: Springer & Verlag; 1998.
- [90] Einasto M, Einasto J, Tago E, Dalton GB, Andernach H. The Structure of the Universe Traced by Rich Clusters of Galaxies. *MNRAS.* 1994;269:301–322.
- [91] Lindner U, Einasto J, Einasto M, Freudling W, Fricke K, Tago E. The structure of supervoids. I. Void hierarchy in the Northern Local Supervoid. *A&A.* 1995;301:329–347.
- [92] Vielva P, Martínez-González E, Barreiro RB, Sanz JL, Cayón L. Detection of Non-Gaussianity in the Wilkinson Microwave Anisotropy Probe First-Year Data Using Spherical Wavelets. *ApJ.* 2004;609:22–34.
- [93] Cruz M, Martínez-González E, Vielva P, Cayón L. Detection of a non-Gaussian spot in WMAP. *MNRAS.* 2005;356:29–40.
- [94] Vielva P. A Comprehensive Overview of the Cold Spot. *Advances in Astronomy.* 2010;2010:1–20.
- [95] Rudnick L, Brown S, Williams LR. Extragalactic Radio Sources and the WMAP Cold Spot. *ApJ.* 2007;671:40–44.
- [96] McEwen JD, Wiaux Y, Hobson MP, Vanderghenst P, Lasenby AN. Probing dark energy with steerable wavelets through correlation of WMAP and NVSS local morphological measures. *MNRAS.* 2008;384:1289–1300.
- [97] Ivezić Ž, Menou K, Knapp GR, Strauss MA, Lupton RH. Optical and Radio Properties of Extragalactic Sources Observed by the FIRST Survey and the Sloan Digital Sky Survey. *AJ.* 2002;124:2364–2400.
- [98] Peebles PJE. *Principles of physical cosmology.* Princeton, N.J.: Princeton University Press; 1993.
- [99] Zehavi I, Weinberg DH, Zheng Z, Berlind AA, Frieman JA, Scocimarro R. On Departures from a Power Law in the Galaxy Correlation Function. *ApJ.* 2004;608:16–24.
- [100] Coles P, Lucchin F. *Cosmology: The Origin and Evolution of Cosmic Structure*, Second Edition. Chichester, England: John Wiley & Son; 2002.
- [101] Zaninetti L. Dynamical Voronoi tessellation. V. Thickness and incompleteness. *A&AS.* 1995;109:71–77.
- [102] Szalay AS, Broadhurst TJ, Ellman N, Koo DC, Ellis RS. Redshift Survey with Multiple Pencil Beams at the Galactic Poles. *Proceedings of the National Academy of Science.* 1993;90:4853–4858.
- [103] Martínez VJ, Arnalte-Mur P, Saar E, de la Cruz P, Pons-Bordería MJ, Paredes S, et al. Reliability of the Detection of the Baryon Acoustic Peak. *ApJ.* 2009;696:L93–L97.
- [104] Okabe A, Boots B, Sugihara K. *Spatial tessellations. Concepts and Applications of Voronoi*

- diagrams. Chichester, New York: Wiley; 1992.
- [105] Heinrich L, Muche L. Second-order properties of the point process of nodes in a stationary Voronoi tessellation. *Math Nachr.* 2008;281(3):350–375.
 - [106] Eisenstein DJ, Zehavi I, Hogg DW, Scoccimarro R, Blanton MR, Nichol RCea. Detection of the Baryon Acoustic Peak in the Large-Scale Correlation Function of SDSS Luminous Red Galaxies. *ApJ* . 2005;633:560–574.
 - [107] Springer MD, Thompson WE. The distribution of products of beta, gamma and Gaussian random variables. *SIAM J Appl Math.* 1970;18:721–737.